# On Neutron Star Pulsars and Polarization

Kartik Tiwari

May 18, 2023

# STATEMENT BY AUTHOR

This dissertation has been submitted in partial fulfillment of requirements for a degree of Postgradute Diploma in Advanced Studies and Research at Ashoka University and is deposited in the Library to be made available to borrowers under rules of Ashoka University.

Brief quotations from this dissertation are allowable without special permission, provided that accurate acknowledgement of source is made. Requests for permission for extended quotation from, or reproduction of this manuscript in whole or in part, may be granted by the Competent Authority of Ashoka University when in his or her judgement the proposed use of the material is in the interests of scholarship. In all other instances, however, permission must be obtained from the author.

Kartik Tiwari

# DECLARATION

I hereby declare that the investigation presented in the thesis has been carried out by me. The work is original and has not been submitted earlier as a whole or in part for a degree/diploma at this or any other Institution/University.

Kartik Tiwari

# Acknowledgements

I am grateful to Prof. Dipankar Bhattacharya for many academic, professional and personal contributions. Having spent a year learning from him in the classroom, during office hours, as his teaching assistant and as his thesis student, Prof. Dipankar has had the single largest contribution in developing my understanding of astrophysics. The breadth and depth of his expertise in an impressively large number of domains provides me an ideal to strive towards on my journey as a physicist.

Throughout my undergraduate education, I have had the fortune to be mentored by many excellent advisors and each of them have contributed in deepening my commitment towards pursuing physics research and equipped me with skills to handle increasingly difficult problems. I thank Prof. Hari Hablani (IIT-Indore), Prof. Miguel Alcubierre (UNAM), Prof. Julian Barbour (Oxford University, formerly), Prof. Pramoda Kumar (Ashoka University) and Prof. Somak Raychaudhury (Ashoka University).

I am grateful to Vipasha Barot for filling my life with warmth and to my many friends for making it incredibly vibrant. I am grateful to my parents, Anuradha and Vineet, for investing incomprehensibly large portions of their lives into my wellbeing. Lastly, I thank the many donors funding Ashoka University who made my college education possible free of cost. I claim with no reserve that the years I spent at Ashoka have been the most transformative and fulfilling academically, creatively, psychologically and spiritually.

# Contents

# Chapter 1

# Introduction

*Strong gravitational effects distort polarization information contained in neutron star emissions. Understanding the distortions precisely is essential to understanding the polarization information which may contain valuable insights about neutron star processes (including hints of new physics). This chapter introduces and contextualizes the problem that the following chapters formalize and proceed to solve. We begin by briefly discussing the astrophysics of neutron stars and aspects of polarimetery. The current chapter concludes by outlining the organization of the remainder of this thesis.*

## 1.1 Neutron Stars

*Neutron Stars* (NS) belong to the family of 'compact objects', the parent category consisting also of White Dwarfs (WD) and Black Holes (BH). Compact objects are the end products of stellar evolution that have ceased active nuclear burning for maintaining structural support. Additionally, such objects (owing to their compactness) differ from main-sequence stars because, at their densities, both the precise role of short-range particle interactions and the macroscopic general relativistic effects become manifest.

Neutron Stars are among some of the most exotic known astrophysical objects whose

interior physics can (in principle) be probed observationally[1]. Further, as is ubiquitous in astrophysical studies, a complete description of neutron star physics often involves ideas from multiple theoretical domains such as high energy physics, nuclear physics, gravitational physics, quantum electrodynamics, etc. Hence, it is no surprise that neutron stars have remained the subject of interest for several research programs. This interest in neutron stars amongst astrophysicists has naturally led to several detailed reviews on the subject [1, 2, 3, 4]. In this section, we will briefly glance at some important developments in the field of neutron star astrophysics.

### 1.1.1 Early History

Arguably, Lev Landau anticipated, even before the discovery of neutrons by James Chadwick, the existence of stars that 'look like giant atomic nuclei'. He later shared this with Niels Bohr and Leon Rosenfeld in Copenhagen in 1932 (also the year when James Chadwick published his discovery of neutrons in *Nature*). An interesting discussion on Landau's involvement in neutron star physics can be found in [5]. A year later, in 1933, Walter Baade and Fritz Zwicky gave a talk in a conference organized by American Physical Society, where they coined the term 'supernova'. Finally, on 15 August 1934, the abstract of their talk was published in *Physical Reviews* with the following claim [1]

> With all reserve we advance the view that supernovae represent the transition from ordinary stars into *neutron stars*, which in their final stages consist of extremely tightly packed neutrons.

The next important milestone was the derivation of the hydrostatic equilibrium with inclusion of general relativistic effects. This was worked out by R. C. Tolman at Caltech and J.R. Oppenheimer and G. M. Volkoff at University of Berkeley and, coincidentally, submitted and published in the same edition of *Physical Review* on 15 February, 1939

---

[1]Black holes are denser but any information about processes inside Schwarzschild radius is irrecoverable

[6, 7]. The *Tolman-Oppenheimer-Volkoff Equation* (discussed in more detail in §1.1.4) provided the starting grounds for investigating various neutron star models. This seminal result launched the (still on-going) hunt for an appropriate equation of state (see §1.1.5).

Initial attempts to observe neutron stars were in X-Ray. Stuart Bowyer's team tried to estimate the size of the x-ray source in crab nebula and concluded that it was too big to be a neutron star [8]. Ironically, they missed detecting the crab nebula pulsar as it is hidden within a pulsar wind nebula [9]. Though some compact x-ray sources had been detected by 1968, their association with neutron stars were not convincing for the majority of the astrophysics community. It was in 1967, almost three decades after the initial conceptualization, Jocelyn Bell discovered the first radio pulsar [10] that was attributed to be a neutron star. She performed this observation using the (then) state-of-the-art radio telescope her doctoral advisor, Anthony Hewish, had constructed at Cavendish Laboratory[2].

Initially, there was disagreement about whether the source of pulsation were rotating white dwarfs or neutron stars. The very small spin period of crab nebula pulsar ($\sim$ 30 milliseconds) provided authoritative evidence to rule out the white dwarf hypothesis. This was because white dwarfs would not be able to survive the strong centrifugal forces generated by rotation as rapid as that of the crab nebula pulsar. Later, the observed slowing down of pulsar periods provided arguments against possible stellar oscillations as pulsar sources because those were expected to be stable in the concerned time-scales. Finally, the verdict on radio pulsars was that they were spinning neutron stars with a strong magnetic field offset from their spin-axis and responsible for producing beamed emissions (like a light-house).

The textbook on neutron stars by Haensel et al. [11] starts with an excellent review of the historical role of neutron star discussions in the broader astrophysics research of

---

[2]It remains controversial for the Swedish Academy to have excluded Jocelyn Bell in the Nobel Prize awarded for the discovery of pulsars in 1974.

20th century.

## 1.1.2  Formation and Evolution

Canonically, two mechanisms for the formation of neutron stars have been proposed.

1. After the final stages of the nuclear burning in main sequence stars, the core is rendered inert and unable to support itself against further gravitational collapse. If the mass of the core falls below the Chandrasekhar limit ($\sim 1.4\ M_\odot$), the star is supported via electron degeneracy pressure. However, if the core mass exceeds the Chandrasekhar limit, it collapses into a neutron star (or, in more massive cases, a black hole).

2. Accretion of matter onto a white dwarf in a binary system, under the appropriate conditions, can lead to the white dwarf accumulating enough matter to exceed the Chandrasekhar limit after its formation and collapse into a neutron star.

It is worth mentioning that, as argued by Bhattacharya [12] on the grounds of observational data in 1991, 'so far, no convincing need for the formation of neutron stars in globular clusters by accretion induced collapse of white dwarfs has been demonstrated'.

Modelling neutron star evolution is largely a question of modelling its magnetic field evolution and its rotation rate evolution (the two being connected in non-trivial ways). Initially, Gunn and Ostriker [13] proposed an argument for field decay due to Ohmic resistance caused by the currents that maintain the field. Such arguments are met with some resistance themselves as the interior of neutron stars are now thought to be highly conducting (superconducting even) leading to currents that practically survive forever [14]. More convincing pieces of observational evidence for magnetic field decays come from velocity measurements of radio pulsars. Assuming most pulsars are born near the galactic center, the ratio of their velocity to the distance from the galactic center provides an estimate for their age. In certain regimes, it has been demonstrated that this 'kinetic

4

age' has correlation with the 'spin-down age' ($\tau \equiv P/2\dot{P}$, where $P$ is the pulsar period and $\dot{P}$ is the rate of change of pulsar period) [15]. Another observational evidence for field decay is that young pulsars often associated with supernova remnants have stronger magnetic fields than old pulsars found in globular clusters or as white dwarf companions. Theoretically, three major physical models are proposed to explain the field decay and, as of yet, none of them provide completely satisfactory solutions [16]. The chapter by Dipankar Bhattacharya and Ganesan Srinivasan in [3] provides a review of observational and theoretical issues in field decay. Discussions of pulsar spin-down and braking can be found in [17, 18, 19].

### 1.1.3   Neutron Star Structure

Neutron stars are roughly divided into three regions- atmosphere, crust and core. However, each of these regions is often further divided into sub-regions as per the choice of the model.

1. *Atmosphere* is thought to be very thin, composed of plasma and is the source of the thermal spectrum of NS emissions. These thermal emissions from the atmosphere carry information about composition, temperature and field geometry of the surface.

2. *Crust* starts off as non-degenerate electron gas and ions but quickly turns into ultra-relativistic strongly degenerate almost ideal electron gas. With increasing density deeper into the star, beta capture increases and nuclei start becoming neutron rich. Towards the inner crust and at the crust-core interface, neutronization reaches a point where nuclei essentially disappear.

3. *Core* is largely composed of neutrons with some small percentage of protons, electrons and muons. Electrons and muons form an ideal fermi gas and protons and neutrons, due to nuclear interactions, acts as interacting Fermi liquids in super-

fluid states. Dozens of hypothesis about the state of matter at the heart of neutron stars have been put forward such as hyperonization (hyperons are baryonic particles with one or more strange quarks), pion condensation (bosonic condensation of pion like excitations), kaon condensation (bosonic condensation of kaon like excitations), etc. but uncertainty prevails.

To arrive at an understanding about NS processes or propose experimentally verifiable claims about NS structure, the general strategy is to first develop theoretical models and then explore their specific features. As one would guess, claims about neutron star structure can be highly model dependent. However, developing any neutron star model would involve solving stellar structure equation governing equilibrium conditions, making a choice of equation of state and providing a description of radiative transfer. We briefly discuss the first two topics in this chapter and the last one in the following chapter.

### 1.1.4 Tolman-Oppenheimer-Volkoff Equation

As hinted earlier, the starting point for understanding neutron star structure is the Tolman-Oppenheimer-Volkoff equation for hydrostatic equilibrium solved in conjunction with a reasonable choice of equation of state. Then, to model physical settings more realistically, one has to arrive at the analog of TOV equation for a fast rotating general relativistic body (discussed again in §4.1.2) and an equation of state that includes sophisticated sub-nuclear interactions. Following is a brief outline of the derivation of stellar structure equations in GR but more rigourous expositions can be found in standard textbooks on general relativity (see §23.4 in [20]) or compact objects (see §6.1 in [11]).

Schwarzschild metric describes the curvature in the exterior regions of spherically symmetric spacetime. However, for solving the stellar structure of stars, we need to start

with a more general metric for spherically symmetric spacetimes.

$$ds^2 = g_{\mu\nu}dx^\mu dx^\nu = -e^{2\Phi}c^2 dt^2 + e^{2\Lambda}dr^2 + r^2(d\theta^2 + \sin^2\theta\, d\phi^2) \tag{1.1}$$

where $\Phi = \Phi(r)$ and $\Lambda = \Lambda(r)$ are some functions which decay to 0 as $r \to \infty$ so that the metric asymptotically approaches metric for Minkowski (flat) geometry. This metric must satisfy the Einstein Field Equations -

$$R_{\mu\nu} - \frac{1}{2}Rg_{\mu\nu} = \left(\frac{8\pi G}{c^4}\right)T_{\mu\nu} \tag{1.2}$$

where information about curvature is captured in Ricci tensor $R_{\mu\nu}$ and Ricci scalar $R = g^{\mu\nu}R_{\mu\nu}$ (i.e. the trace of Ricci tensor). $T_{\mu\nu}$ captures information about the distribution of mass and energy which serves as the source of curvature. We assume that neutron star matter is a non-viscous perfect fluid with total energy density $\epsilon$. For such a fluid, all stress components are zero except for isotropic pressure $P$. This is a permissible approximation in the case of neutron stars because the shear stress produced by elastic strain or magnetic field is much smaller than pressure. Thus, we can represent the stress-energy-momentum tensor as

$$T_{\mu\nu} = (P + \epsilon)u_\mu u_\nu - Pg_{\mu\nu} \tag{1.3}$$

where $u_\mu, u_\nu$ are fluid 4-velocities. Note that both $P$ and $\epsilon$ are defined in a local co-moving inertial frame. Finally, for assembling the structure equations, we require the law of local energy-momentum conservation

$$T^{\mu\nu}_{;\nu} = 0 \tag{1.4}$$

where the semi-colon in subscript refers to the covariant derivative along $x^\nu$ compo-

7

nent. One can further show that $\Lambda(r)$ can be written in terms of another function $m(r)$

$$e^{2\Lambda(r)} = \left(1 - \frac{Gm(r)}{rc^2}\right)^{-1} \tag{1.5}$$

where $m(r)$ refers to the gravitational mass enclosed by a sphere of radius $r$. It is important to note that in the case of neutron stars, gravitational mass $m(r)$ tends to be smaller than the baryon mass (or rest mass) due to gravitational mass defect [21]. Finally, on calculating all the required components of the Ricci tensor and using field equations and conservation equations, one arrives at the following set of first-order coupled differential equation for the stellar structure -

$$\frac{dP}{dr} = -\frac{G\rho(r)m(r)}{r^2}\left(1 + \frac{P(r)}{c^2\rho(r)}\right)\left(1 + \frac{4\pi P(r)r^3}{m(r)c^2}\right)\left(1 - \frac{2Gm(r)}{c^2 r}\right)^{-1} \tag{1.6}$$

$$\frac{dm}{dr} = 4\pi r^2 \rho(r) \tag{1.7}$$

$$\frac{d\Phi}{dr} = \frac{1}{c^2\rho(r)}\left(1 + \frac{P(r)}{c^2\rho(r)}\right)^{-1}\frac{dP}{dr} \tag{1.8}$$

where $\rho(r) = \epsilon(r)/c^2$ is mass density. Eq. (1.6) is the complete form of the famous TOV-equation which reduces to the following in non-relativistic regimes ($P << \rho c^2$ and $Pr^3 << mc^2$)

$$\frac{dP}{dr} = -\frac{Gm\rho}{r^2} \tag{1.9}$$

$$\frac{dm}{dr} = 4\pi r^2 \rho \tag{1.10}$$

On comparing pressure gradients with and without relativistic corrections we find that, as one goes deeper into the star, pressure rises more rapidly than Newtonian theory would suggest. Additionally, as pressure increases, the relativistic correction term due to pressure becomes more dominant. Hence, GR can lead to further stellar collapse in the cases where Newtonian analysis would predict a hydrostatic equilibrium.

To describe the neutron star structure, we started with 4 unknown functions - two

in the metric $\Phi(r)$ and $m(r)$ (or originally $\Lambda(r)$) and two in energy-momentum tensor $P(r)$ and $\rho(r)$ (or originally $\epsilon(r)$). To close the system, we need to supplement the three differential equations with an equation of state which connects pressure with density[3].

### 1.1.5  Equation of State

The Equation-of-State (EoS) is constituted via microscopic considerations and an appropriate EoS of neutron stars would carry information about particle interactions at extremely high densities. At such densities (higher even than the nuclear density), strange baryons and deconfined quarks could appear providing conditions that are difficult to replicate in laboratories. However, the EoS also affects the stellar equilibrium sufficiently enough to lead to macroscopic changes in the mass-radius relations and observing mass and radius of neutron stars can constrain proposals in particle and high-energy physics. This is a rapidly advancing field, one that attracts astrophysicists and nuclear physicists alike. Shapiro et al. [1] has an excellent discussion about some equations of states but it has significantly grown out-dated since its publication in early 1980s. Haensel et al. [11] has a more recent textbook dedicated primarily towards providing pedagogical expositions of various Neutron Star EoS. Though it ignores the possible appearance of quark matter and only discusses nucleonic and hyperonic degrees-of-freedom, the most up-to-date scientific review at the moment is Burgio et al. [22].

## 1.2  Polarization

Having discussed some general elements of neutron star physics, we now focus our attention to polarization of the NS radiation. This section primarily motivates the need for neutron star polarimetery and introduces Stokes parameters for quantifying polariza-

---

[3]Since neutron stars cool rapidly via neutrino flux soon after their formation, their actual temperatures are much smaller than their Fermi temperatures. Therefore, it is reasonable to ignore thermal contributions while calculating pressure. Some cases where such approximations fail would include very young neutron stars and neutron star atmosphere

tion. Mechanisms generating linearly polarized radiation in neutron stars are discussed in §2.1 Experimental methods for measuring X-Ray polarization and polarimetery missions are discussed later in §4.2.

### 1.2.1 Why Neutron Star Polarimetery

A family of reasons to study the information contained in the polarimetery data of neutron star emissions could be to arrive at more refined models for neutron star physics. More specifically

1. Studying the polarization of neutron star radiation might help us understand better the radiative transfer processes that produce the radiation.

2. We expect regions of neutron stars to be have differential opacity as a function of the polarization mode of the passing radiation.

3. Since polarization is a function of magnetic field distribution and the apparent field geometry changes periodically for pulsars, pulsations in polarization data reveal information about the magnetic field distribution.

4. Bending of light around neutron stars due to their compactness factor reduces the linear polarization as more of the surface (with differently polarized emissions) becomes visible to the observer. Therefore, polarization can provide new insights on mass-to-radius ratio measurements.

Alternatively, one might want to study polarization in neutron star emissions to test theoretical predictions which are difficult to test in terrestrial laboratory conditions. For example, in certain neutron stars (called magnetars) that display the strongest known magnetic fields in the universe reaching up to $10^{15}$ Gauss, quantum electrodynamics predicts vacuum to act as a birefringent medium. This is a famous claim that astrophysicists have been trying to test using magnetar observations [23].

### 1.2.2  Stokes Parameters

To build up to the formalism of Stokes parameters for describing polarization of electro-magnetic waves, a natural place to begin would be Maxwell's equations in the absence of sources

$$\nabla . E = 0 \tag{1.11}$$

$$\nabla . B = 0 \tag{1.12}$$

$$\nabla \times E = -\frac{\partial B}{\partial t} \tag{1.13}$$

$$\nabla \times B = \mu_0 \epsilon_0 \frac{\partial E}{\partial t} \tag{1.14}$$

By making use of the vanishing divergences and combining the two curl equations, we find that each Cartesian component of $\vec{E}$ and $\vec{B}$ follow the wave equation

$$\nabla^2 u = \frac{1}{c^2} \frac{\partial^2 u}{\partial t^2} \tag{1.15}$$

where $c$ is the speed of light. The solution for the wave equation are famously composed of functions of the following form

$$u(\vec{x}, t) = \exp(i\vec{k}.\vec{x} - \omega t) \tag{1.16}$$

with the frequency $\omega$ and the magnitude of the wave vector $k$ being related by the simple dispersion relation $k = \omega/v$, where $v$ is the phase velocity of propagation. Further, it is easy to show that perturbations in electric and magnetic fields propagate as transverse waves and remain perpendicular to each other [24]. Therefore, we can construct a set of orthogonal basis $\hat{e}_1, \hat{e}_2, \hat{n}$ where $\hat{n}$ is the unit vector pointing in the direction of the wave-vector $\vec{k}$.

The most general homogeneous plane wave solution (now looking at electric field)

would be the superposition of the perturbations in $\hat{\epsilon}_1$ and $\hat{\epsilon}_2$ directions

$$\vec{E} = (E_1\hat{\epsilon}_1 + E_2\hat{\epsilon}_2)e^{i(k\hat{n}.\vec{x}+\omega t)} \tag{1.17}$$

where the direction of wave propagation is along the z-axis. Both $E_1$ and $E_2$ are to be taken as complex amplitudes to allow for a phase difference between the two constituent waves along $\hat{\epsilon}_1$ and $\hat{\epsilon}_2$ - henceforth referred to as the two linear polarization modes.

If $E_1$ and $E_2$ have the same phase, the electromagnetic wave is *linearly polarized* with the polarization vector making an angle of $\theta = \tan^{-1}(E_2/E_1)$ with $\hat{\epsilon}_1$. If $E_1$ and $E_2$ have some phase difference, we get *elliptical polarization*. A special case of elliptical polarization would be when the phase difference is exactly $\pi/2$ leading to *circular polarization*. If we assume constant magnitude $E_0$ for both $E_1$ and $E_2$, then linearly polarized light would be of the form

$$\vec{E} = E_0(\hat{\epsilon}_1 \pm \hat{\epsilon}_2)e^{i(\vec{k}.\vec{z}-\omega t)} \tag{1.18}$$

$$E_x = E_0\cos(\vec{k}.\vec{z} - \omega t) \tag{1.19}$$

$$E_y = \mp E_0\cos(\vec{k}.\vec{z} - \omega t) \tag{1.20}$$

In the case of circular polarization, we can define two basis in terms of the positive helicity (counter-clockwise rotation) and negative helicity (clockwise rotation)

$$\epsilon_\pm \equiv \frac{1}{\sqrt{2}}(\epsilon_1 \pm \epsilon_2) \tag{1.21}$$

If we can write $\vec{E}(z,t)$ in terms of either the linear polarization bases $(\epsilon_1,\epsilon_2)$ or the circular polarization basis $(\epsilon_+,\epsilon_-)$ then we know the polarization contents of the wave. However, in practice we encounter the inverse problem of observing a beam of light and having to extract its polarization components along the basis. In 1851, G. G. Stokes [25]

proposed a way to do exactly this[4].

On getting the dot product of $\vec{E}$ with $\hat{\epsilon}_1$, $\hat{\epsilon}_2$, $\hat{\epsilon}_+$ and $\hat{\epsilon}_-$ we can get the polarization contribution on x-axis, y-axis, positive helicity and negative helicity. If we represent each of these separately as an amplitude and phase, we can write

$$E_1 = a_1 e^{i\delta_1} \tag{1.22}$$

$$E_2 = a_2 e^{i\delta_1} \tag{1.23}$$

$$E_+ = a_+ e^{i\delta_+} \tag{1.24}$$

$$E_- = a_- e^{i\delta_-} \tag{1.25}$$

This equips us to define four stokes parameters in the following way

$$s_0 = |\hat{\epsilon}_1.\vec{E}|^2 + |\hat{\epsilon}_2.\vec{E}|^2 = a_1^2 + a_2^2 \tag{1.26}$$

$$s_1 = |\hat{\epsilon}_1.\vec{E}|^2 - |\hat{\epsilon}_2.\vec{E}|^2 = a_1^2 - a_2^2 \tag{1.27}$$

$$s_2 = 2\text{Re}|(\hat{\epsilon}_1.\vec{E})^*.(\hat{\epsilon}_2.\vec{E})| = 2a_1 a_2 \cos(\delta_2 - \delta_1) \tag{1.28}$$

$$s_3 = 2\text{Im}|(\hat{\epsilon}_1.\vec{E})^*.(\hat{\epsilon}_2.\vec{E})| = 2a_1 a_2 \sin(\delta_2 - \delta_1) \tag{1.29}$$

The four scalars quantities are often referred by different labels in different sources. In this document, hereon, we will adopt the convention that calls the four stokes parameters $s_0 = I, s_1 = Q$, $s_2 = U$, and $s_3 = V$. We can observe that $I$ parameter is essentially the total intensity of the wave. $Q$ parameter captures how much linear polarization in one axis differs from the orthogonal direction. $U$ and $V$ provide information about the phase difference. Note that these can be equivalently written in terms of the circular polarization basis $(\hat{\epsilon}_+, \hat{\epsilon}_-)$ and in that case $Q$ and $U$ carry phase information and $V$ captures the difference in linear polarization along the two directions.

The four stokes parameters are obviously not independent of each other as they are

---

[4]This old technique was brought to fame much later after its discovery by Chandrasekhar

constructed from merely three quantities. In the case of quasi-monochromatic or non-coherent light beams, the stokes parameter must obey the general condition

$$I^2 \geq Q^2 + U^2 + V^2 \tag{1.30}$$

which becomes an equality in the case of monochromatic light.

The relation of Stokes parameters to the polarization ellipse can be further understood by noting the following relations [26]

$$Q = I p_L \cos(2\psi) \cos(2\chi) \tag{1.31}$$

$$U = I p_L \cos(2\psi) \sin(2\chi) \tag{1.32}$$

$$V = I p_L \sin(2\psi) \tag{1.33}$$

where $\chi$ is the angle between major axis of the polarization ellipse and the x-axis of the reference frame in which the polarization ellipse is defined and $\psi$ is the angle between major axis of the polarization ellipse and the chord joining major and minor axis. Further, $p$ corresponds to the degree of linear polarization defined as

$$p_L = \frac{1 - e^2}{1 + e^2} \tag{1.34}$$

where e is the eccentricity (i.e. ratio of major and minor axis) of the polarization ellipse. These results would be helpful in calculating the polarization transport through curved spacetime in §2. Most processes in astrophysics produce linearly or highly linearly polarized light (i.e. $\psi = 0$). So, we will focus our attention only on parameters $Q = I p_L \cos(2\chi)$ and $U = I p_L \sin(2\chi)$ in the following discussions.
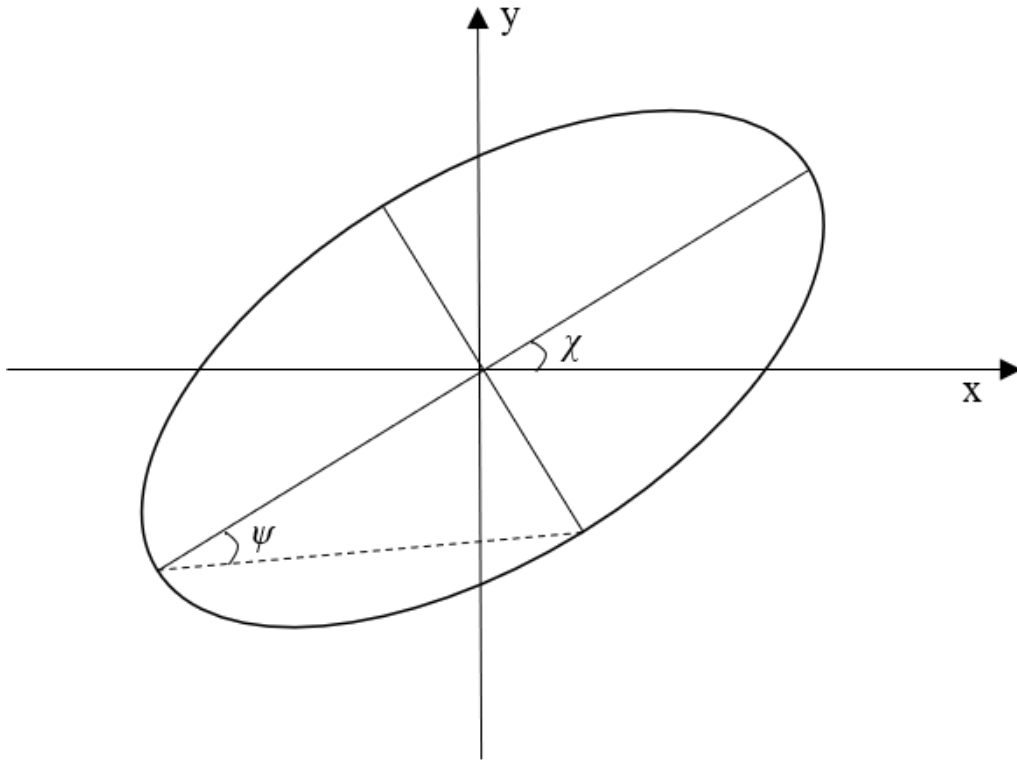
Figure 1.1: Polarization ellipse and its characteristic angles.

## 1.3 Project Outline

The goal of this thesis is to understand how gravitational effects affect the polarization information that we expect from neutron stars. The rest of the chapters are organized in the following manner. §2 goes into details of the gravitational calculations and approximations that power the polarization transport code. §3 illustrates and explains the results generated by the polarization transport code. Finally, §4 discusses the directions in which the project can be extended, both in terms of including new physics and streamlining the simulation-to-observation pipeline. The appendix presents a top-level user-guide for running the polarization transport code.

# Chapter 2

# Gravitational Effects and Pulsar Polarization

*This chapter begins with a discussion on polarization features of neutron star emissions. Then, we derive the photon propagation equation in Schwarzschild and discuss the well-known Beloborodov approximation to the exact solution. A modification to improve the performance of Beloborodov approximation is introduced before moving onto deriving the polarization transport solutions. We end this chapter with a schematic algorithm to generate polarization pulse profiles which is followed by the Polarization Transport Code to generate the results presented in the next chapter.*

## 2.1   Polarization of Neutron Star Emissions

Calculations in this chapter borrow pieces from the literature on neutron star's atmospheric emissions in X-Ray [27, 28, 29] and polarization in high energy environments [30, 31, 32]. We begin by assuming a strong enough magnetic-field $|\vec{B}| > 10^{10}G$ such that the electron cyclotron energy is greater than or equal to the X-ray photon energies (ranging from 100eV to 100KeV). Recall that the expression for electron cyclotron energy

is

$$E_{B_e} = \frac{\hbar e B}{m_e c} = 11.6 \left( \frac{B}{10^{12} G} \right) \tag{2.1}$$

where $e$ is the electron charge, $m_e$ is electron mass, $B$ is the magnetic field strength and $\hbar$ is the reduced Planck's constant. In general, one computes polarization of anisotropic emissions by solving a system of four transport equations for the Stokes parameters. However, it can be shown that in the aforementioned strong magnetic field approximation, one can employ a considerably simpler method of solving only two transport equations for intensities of normal mode (NM) waves [32], each experiencing a different level of opacity through NS atmosphere. Intensity of these two modes - ordinary $I_o$ and extraordinary $I_e$ - sum up to the total intensity of the received radiation. Ordinary mode is polarized parallel to the local magnetic field and extraordinary mode is polarized perpendicular to the local magnetic field. $I_o$ and $I_e$ can be computed using a radiative transfer model for NS atmosphere [33]. Since we are more concerned with how polarization gets affected by gravity, we will not investigate radiative transfer models in much detail.

The intensity $I$ and Stokes parameters $Q$ and $U$ at a region of neutron star surface can be expressed as (see §4 of [32])

$$I = I_o + I_e \tag{2.2}$$

$$Q = (I_o - I_e) p_L \cos 2\chi_o \tag{2.3}$$

$$U = (I_o - I_e) p_L \sin 2\chi_o \tag{2.4}$$

where $\chi_o$ is defined in Fig. 1.1 as the angle between the major axis of the polarization ellipse of the ordinary mode and the x-axis of the reference frame in which Stokes parameters are being considered. The degree of linear polarization $p_L$ is also what was introduced in Eq. 1.34 in terms of the eccentricity of the polarization ellipse. Further,

in dipole approximation, we can express the degree of linear polarization for normal modes as [32]

$$p_L = \frac{|q|\sin^2\theta_B}{\sqrt{4\cos^2\theta_B + q^2\sin^4\theta_B}} \tag{2.5}$$

where $\theta_B$ is the angle between the wave-vector $\hat{k}'$ of the outgoing photon and the magnetic field $\vec{B}$ at the point of emission and $q$ is an angle-independent but photon-energy dependent parameter fixed by the Hermitian components of the polarizability tensor (defined in coordinates where polar axis is aligned with the magnetic field). Assuming we are concerned with completely ionized hydrogen plasma and electron-positron vacuum polarization is ignored, the parameter can be shown to be [34]

$$q = \frac{E'^2(E_{B_e}^2 + E_{B_i}^2 - E_{B_e}E_{B_i}) - E_{B_e}^2 E_{B_i}^2}{E'^3(E_{B_e} - E_{B_i})} \tag{2.6}$$

where $E'$ is the photon energy as measured at the location of emission and

$$E_{B_i} = \left(\frac{m_e}{m_p}\right)E_{B_e} = 6.32 \times 10^{-3}\left(\frac{B}{10^{12}G}\right)KeV$$

is the ion cyclotron energy. For photon energies much greater than ion cycltron energy $E_{B_i}$, $q$ parameter approaches $E_{B_e}/E'$ and $p_L$ remains close to 1 for a wide range of $\theta'$ values. Within these approximations, the angle $\chi_o$ coincides with the azimuthal angle of the magnetic field in a reference frame with polar axis parallel to the wave-vector[1] $\hat{k}'$. This follows directly from the fact that ordinary modes are linearly polarized parallel to the magnetic field.

In a sense with Eq. (2.4)-(2.6) and an emission model for the normal modes, we have enough information to compute the local polarization properties of a neutron star.

---

[1]We introduce a prime in the wave-vector $\hat{k}$ in prior anticipation of a difference between rectilinear observed trajectory and a 'true' curved trajectory. Similarly, we introduce a prime in photon energy $E$ in anticipation of the distinction between observed red-shifted energy and energy at the time of emission.

However, gravitational effects distort this polarization information and understanding these distortions precisely is an important step towards bridging our theoretical radiative transfer modelling of NS atmospheric emissions and observational data from polarimetery of isolated X-ray pulsars.

## 2.2   Expected Distortion

Qualitatively, due to gravitational effects, we can already guess what could be the possible effects on the observed polarization. Following are the major two effects we expect

1. Due to gravitational lensing, we would see more of the neutron star surface at once. Light rays from the regions of the star which would be 'behind' the simple projection of the surface with only rectilinear rays permitted would also start contributing once the rays are allowed to bend around the star and reach the observer. However, we observe neutron stars as point sources with no geometrical span and the observed polarization is an integration over the complete visible surface. Therefore, more regions of the star would contribute towards the total polarization due to the compactness.

2. Secondly, as the light rays bend around the neutron star, the polarization of light itself reorients geometrically in space. Therefore, the Stokes parameter of the emitted ray of light transferred to the observer would not be the same with and without general relativistic effects. The change in the polarization would be function of how much a certain ray has to bend to reach the observer.

To make both of these effects precise, we need to calculate how light rays propagate in the spacetime around a neutron star, what image of the surface is projected onto an observer at infinity and how the polarization vector changes during transport phase before integrating over the entire visible surface. Once we know how to do this, we can create a polarization map on the neutron star surface and perform these calculations for

each spin phase. This would generate pulse profiles for the neutron star flux in a given polarization mode.

## 2.3 Photon Propagation in Schwarzschild

To perform the above mentioned calculations, we assume that the spacetime is described by the exterior Schwarzschild solution. This is a simplifying assumption but modelling with further sophistication, though computationally demanding due to lack of closed form GR solutions, could in principle be analysed similarly (see §4.1.2).

### 2.3.1 Exact Trajectories

The first step is to understand how light behaves outside neutron stars and this is done by calculating null-geodesics $ds^2 = 0$ in Schwarzschild spacetime. We start with writing the spacetime interval in the following choice of coordinates

$$ds^2 = -g_{tt}dt^2 + g_{rr}dr^2 + r^2(d\theta^2 + \sin^2\theta d\phi^2) \tag{2.7}$$

where $g_{tt} = g_{rr}^{-1} = (1 - 2GM/c^2 r)$. For null-geodesics, proper time $d\tau$ is zero and cannot be used to write equations of motion. There are two ways around it. One can use an arbitrary parameter $\lambda$ to perform the calculations or one could derive the equations for the massive particles and take mass going to zero limit. We shall proceed with the former approach (similar to §9.4 in Hartle [35]).

Deriving the photon-propagation equation is greatly simplified by exploiting the symmetries and conserved quantities of the problem. In the static spherically symmet-

ric spacetime which is independent of $t$ and $\phi$ coordinates, we have two Killing vectors

$$\vec{\xi} = (1, 0, 0, 0) \tag{2.8}$$

$$\vec{\eta} = (0, 0, 0, 1) \tag{2.9}$$

Therefore, the following two dot products define the conserved quantities

$$e \equiv -\vec{\xi}.\vec{u} = \left(1 - \frac{2GM}{c^2 r}\right) \frac{dt}{d\lambda} \tag{2.10}$$

$$l \equiv \vec{\xi}.\vec{u} = r^2 \sin^2 \theta \frac{d\phi}{d\lambda} \tag{2.11}$$

We call $e$ the conserved energy per unit rest mass and $l$ the conserved angular momentum per unit rest mass. Further, for brevity, $dx^\mu/d\lambda$ would be referred to as $u^\mu$

Another equation is provided by the dot product of the photon four-velocity[2]

$$\vec{u}.\vec{u} = g_{\mu\nu} \frac{dx^\mu}{d\lambda} \frac{dx^\nu}{d\lambda} = 0 \tag{2.12}$$

Since angular momentum $l$ is conserved, the orbit is confined onto a plane. We can set our coordinates such that the orbital plane corresponds to $\theta = \pi/2$. This simplifies the summation

$$-\left(1 - \frac{2GM}{c^2 r}\right) (u^t)^2 + \left(1 - \frac{2GM}{c^2 r}\right)^{-1} (u^r)^2 + r^2 (u^\phi)^2 = 0 \tag{2.13}$$

We can substitute $u^t$ and $u^\phi$ into (2.13) in terms of the conserved quantities (2.11). This yields

$$-\left(1 - \frac{2GM}{c^2 r}\right)^{-1} e^2 + \left(1 - \frac{2GM}{c^2 r}\right)^{-1} \left(\frac{dr}{d\lambda}\right)^2 + \frac{l^2}{r^2} = 0 \tag{2.14}$$

---

[2]In case of massive particles, 0 on the RHS gets replaced with $-1$ and the arbitrary parameter can be taken as proper-time $d\tau$.

Or, on multiplying with $g_{tt}$ and rearranging

$$\left(\frac{dr}{d\lambda}\right)^2 = e^2 - \frac{l^2}{r^2}\left(1 - \frac{r_G}{r}\right) \tag{2.15}$$

where $r_G \equiv 2GM/c^2$. Since we know $d\phi/d\lambda = l/r^2$ (for $\theta = \pi/2$), we can eliminate the arbitrary parameter from the (2.15) and write

$$\left(\frac{dr}{d\phi}\right)^2 = \frac{r^4}{l^2}\left(e^2 - \frac{l^2}{r^2} + r_G\frac{l^2}{r^3}\right) \tag{2.16}$$

A key distinction between massive and massless trajectories in Schwarzschild is that null-geodesics only depend on the ratio of $e$ and $l$ while trajectories of massive particles are impacted by each of these conserved quantities individually. This is because of the freedom in the choosing the affine parameter $\lambda$. Physical predictions should not depend on the parameterization and rescaling $\lambda$ rescales both $e$ and $l$ in the same way.

Since it is only the ratio that matters, we can choose our units such that $e$ is set to 1 and $l$ becomes $\bar{l}$. To avoid writing the bar frequently, hereon, every instance of $l$ would be referring to $\bar{l}$. So, the final photon propagation equation for Schwarzschild geometry is

$$\boxed{\left(\frac{dr}{d\phi}\right)^2 = \frac{r^4}{l^2}\left(1 - \frac{l^2}{r^2} + r_G\frac{l^2}{r^3}\right)} \tag{2.17}$$

If we define a quantity $b \equiv |l/e|$ then $b$ serves as the *impact parameter*.

$$b \equiv \frac{r^2 d\phi/d\lambda}{dt/d\lambda} = r^2\frac{d\phi}{dt} \tag{2.18}$$

If we take the limit $r \to \infty$ then we can approximate $\phi \approx d/r$ where $d$ is the distance from the $x$ axis (defined such that source of curvature is at the origin and travelling light ray is

parallel to X-axis at infinity). Further,

$$\frac{d\phi}{dt} = \frac{d\phi}{dr}\frac{dr}{dt} = \frac{d}{r^2}$$ (2.19)

Therefore,

$$b = d$$ (2.20)

Depending on the choice of units, for the impact parameter to have the dimensions of length, we include velocity $c$ in the definition (i.e. $b \equiv |l/ce|$). Due to our re-scaling, $l$ itself is the impact parameter and it decides the nature of the trajectory. Some example trajectories have been displayed in Fig. 2.1. Though we have integrated numerically (as is the case generally), it is worth noting that the photon trajectory equation was solved in terms of elliptic functions in 2014 [36].

A slightly non-trivial aspect of integrating the photon propagation equation is the fact that the ODE flips sign during integration. The ODE carries a negative sign as the ray is integrated from a source at infinity towards the source of curvature ($r$ is decreasing). However, once it reaches the closest point (i.e. derivative $dr/d\phi$ approaches zero), the ODE changes sign and the ray starts moving away from the source of curvature (assuming it started with a sufficiently large impact parameter $l$). If the impact parameter $l$ at infinity is less that $l_{min} = 3\sqrt{3}r_G$ then the photon cannot escape the potential well of the gravitating body.

### 2.3.2 Beloborodov Approximation

Each patch on the neutron star surface emits light rays in all directions. For each patch, we are interested in rays that are emitted at an angle such that after lensing they reach an observer situated at a particular location. Integrating all such rays from the surface to the observer is wasteful as we would be integrating many other rays that do not reach the
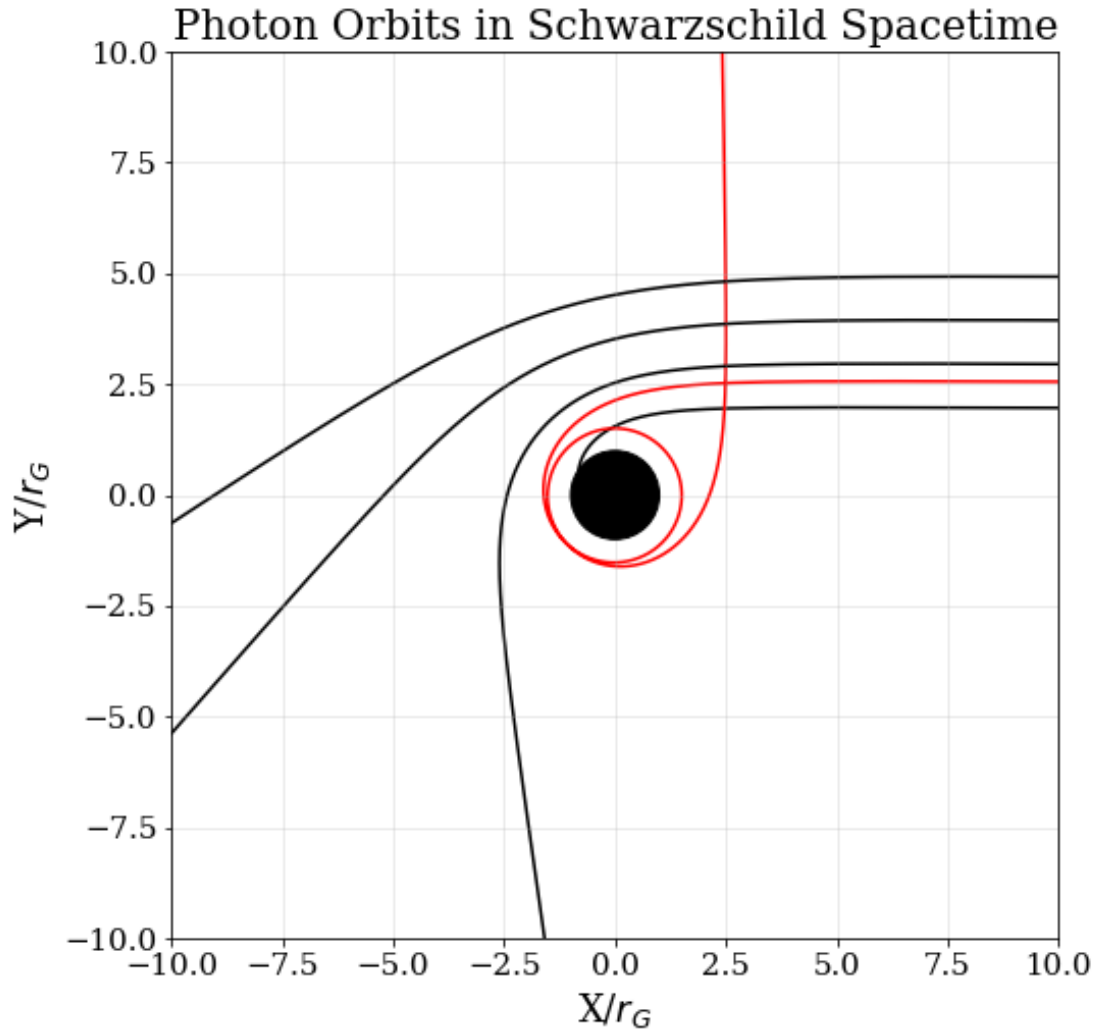
Figure 2.1: Multiple photon trajectories around an $r = r_G$ objec with varying impact parameters. The red trajectory has an impact parameter $l/r_G$ close to $l_{min} = 3\sqrt{3}r_G$ and it circles around the black hole multiple times before escaping to infinity. The displayed trajectories were integrated using a fourth-order Runge-Kutta integrator.

observer. Instead, we integrate multiple photon trajectories from an observer at infinity

with varying impact parameter slightly. These trajectories would then hit the source of

curvature located at the center of our coordinate frame at a particular location and a

particular angle. If we look at longitudinal cross section of the neutron star, then the

location where photon trajectory meets the surface can be characterized by the latitude

angle $\phi$. Further, the angle at which the trajectory hits the surface is simply the angle at which a photon would have to escape that surface patch to reach the observer. This angle we define as $\alpha$.

In absence of gravitational effects, the relation between $\phi$ and $\alpha$ would be simply $\phi = \alpha$. However, due to lensing, we find there is a bending angle $\beta = \phi - \alpha$ that becomes relevant and the relation between $\phi$ and $\alpha$ becomes non-trivial. The emission angle $\alpha$ is an important quantity to know because it governs how much of the neutron star surface would be visible to us. At $\alpha = 90^o$, the ray grazes the surface and reaches the observer. On the other hand, if $\alpha$ exceeds $90^o$, then the photon only reaches the observer if it travels through the surface of the neutron star, which is not physical. Additionally, knowing the $\alpha$ associated with each surface patch tells us how much that surface patch contributes towards the total flux observed at observer's location. If a patch emits a flux of $F_0$ then the contribution towards total flux is $F_0 \cos(\alpha)$. Therefore, we require a relation between $\phi$ and $\alpha$ to be able to predict the contribution of a surface patch from the knowledge of its location. Finding this relation, however, requires numerically integrating each relevant trajectory.

Numerically, ray-tracing trajectories to each (discretized) patch of the neutron star surface for each spin-phase is extremely computationally heavy and has poor scaling properties. These computational demands become extremely restrictive when one tries to write inference codes because Bayesian inference over some high-dimensional parameter space itself is a very hardware heavy procedure (discussed further in §4.1.4).

Beloborodov in 2003 proposed an excellent approximation that by-passes the need for explicit ray tracing and has become a standard approximation in lensing calculations [37]. The approximation takes the following form

$$(1 - \cos \alpha) = (1 - \cos \phi)\left(1 - \frac{r_G}{R}\right) \tag{2.21}$$

where $R$ is the radius of the neutron star. It has been shown that the approximation

maintains high-accuracy for $R > r_G$ and is, therefore, applicable in neutron star contexts. The reason for high-accuracy of 2.21 cannot simply be understood as a linear expansion in terms of a parameter $u \equiv r_G/R$ (such an approach leads to a much less accurate approximation). Instead, as explained in [37], the way to understand the remarkable accuracy of the approximation is by defining a small parameter $x \equiv 1 - \cos\alpha$ and expanding $y \equiv 1 - \cos\phi$ in terms of a power-series $x^k$. On doing so and simplifying the algebra, we find

$$y = \frac{x}{1-u} - \frac{u^2}{112}\left(\frac{x}{1-u}\right)^3 - \frac{u^2}{224}\left(\frac{5}{3} - u\right)\left(\frac{x}{1-u}\right)^4 + \mathcal{O}(x^5) \qquad (2.22)$$

Notice that there is no $x^2$ term in the expansion. The corrections are only in higher power with small coefficients that suppress them. Though there is no sufficiently satisfactory method to motivate such an approximation from first-principles, following results demonstrate that it remains fairly accurate for a wide range of relevant angles.

We test the accuracy of Beloborodov's approximation for a given compactness value by ray-tracing a photon trajectory from infinity until the radial distance from the center of the gravitating body becomes equal to the radius of the neutron star $R$. Then, we check the last location of the photon to find its location on the surface $\phi$. Finally, emission angle $\alpha$ can be found using the dot product of the unit radius vector and the direction of photon 3-velocity at radius R

$$\cos\alpha = \frac{\hat{r}.\vec{u}_3(R)}{|\vec{u}_3(R)|} \qquad (2.23)$$

On repeating this process for multiple rays of varying impact parameters, we get a trend between angle of emission and surface location for all rays escaping the longitudinal cross section of the neutron star that reach the observer (Fig. 2.3). This trend can then be compared against what Eq. (2.21) approximates.

The comparison of exact and approximate results for $R = 2.5r_G$ in Fig. 2.4 shows
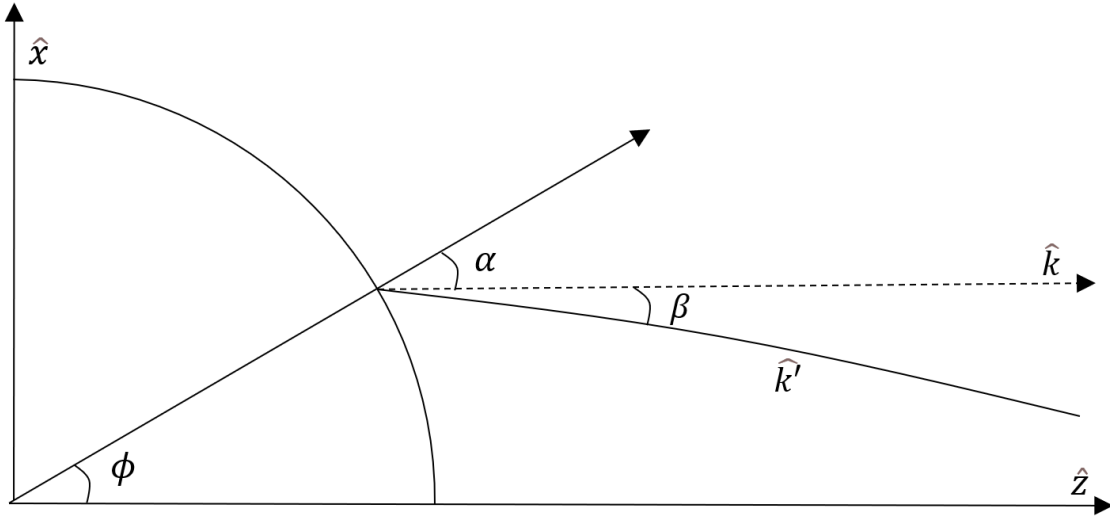
Figure 2.2: Emission angle $\alpha$ measured with respect to the local normal $\hat{r}$ on neutron star surface. Note that in this figure $\hat{z}$ points towards line of sight, instead of $\hat{x}$. This is explained in §2.4

that the relative errors remain under 2% for almost entirety of the range that we are concerned with. A brief point to note, while reading Fig. 2.4, is that the latitude of a surface patch is equal to the angle between the line of sight and the radial vector because we assume the observer to be infinitely far from the neutron star (we see neutron stars as point like sources with no geometrical span). Therefore, all rays connecting the surface to the observer are parallel to each other.

### 2.3.3 Modified Beloborodov Approximation

In the trend analysis presented in [37], it is clear that the Beloborodov approximation drops in accuracy as one approaches more compact neutron stars (i.e. $R = 2r_G$). However, the residues post-approximation, when compared against the exact trajectories, can be fit through a third order polynomial very well. The coefficients of the third-order polynomial depends on the trend of the residues with respect to angle $\phi$ which in turn depends on the compactness of the neutron star. If one computes exact trajectories for a series of compactness values and observes the trend of the polynomial coefficients that
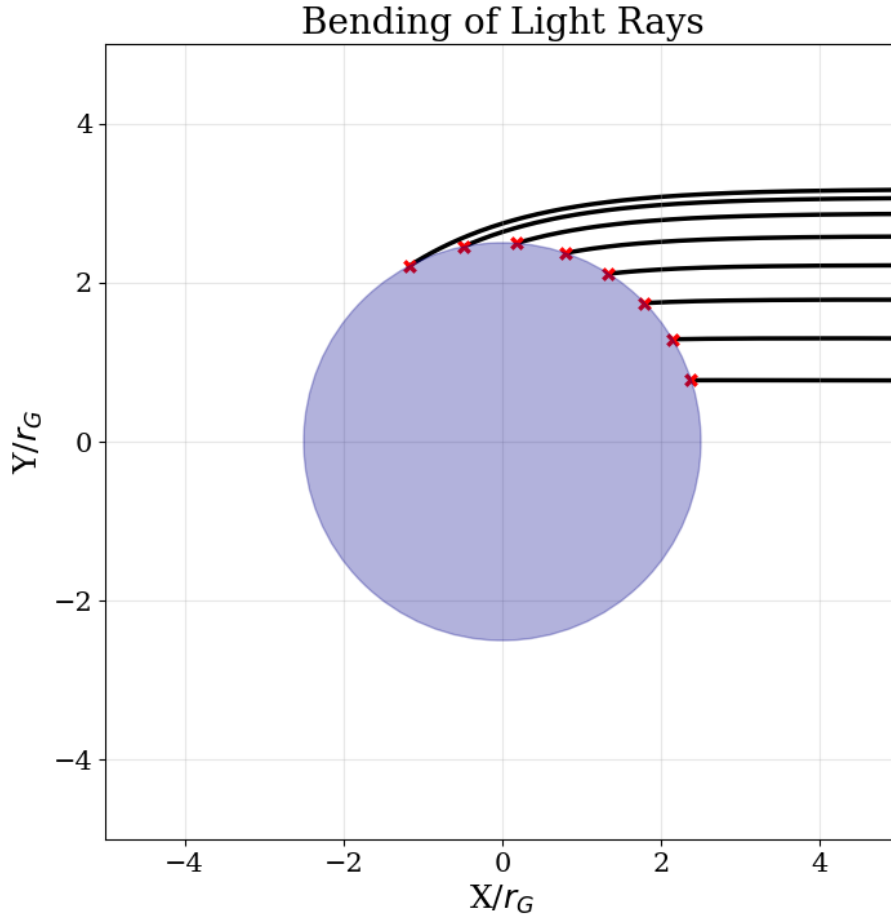
Figure 2.3: Photon trajectories for some impact parameters reaching neutron star surface integrated to find relation between emission angle $\alpha$ and surface location $\phi$.

best fit the residues, one realizes that the trend in coefficients itself is modelled well by a third-order polynomial of the following type.

$$y = A(R)x^3 + B(R)x^2 + C(R)x + D(R) \tag{2.24}$$

We performed these computations and the trend in the coefficients, along with the best-fit polynomial, is displayed in Fig. 2.5. Each correction coefficient is then a function parameterized by four constants. The one-time computation of these twelve constants which can be done with minimal costs (e.g. 5 compactness values and 80 rays for each

Comparing Beloborodov Approximation
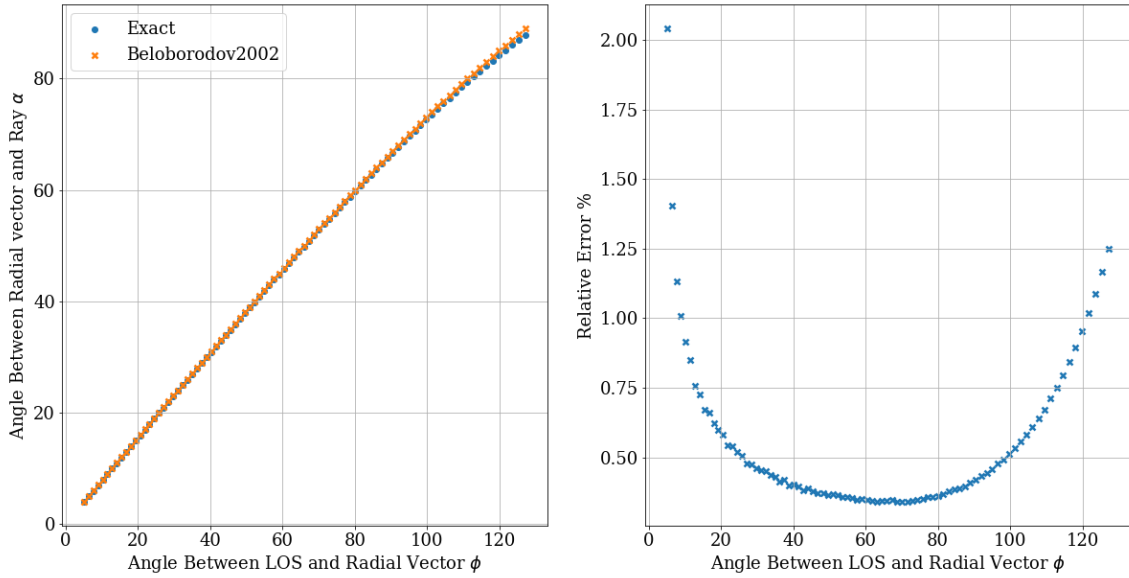with Exact Results

Figure 2.4: Comparing the exact and approximate relations between emission angle $\alpha$ and emission latitude $\phi$

compactness) then provides us a fast improvement over Beloborodov's original approximation. Some of these results have been presented in Fig. 2.6 and 2.7 (Y-axis in top two quadrants in these figures is represented in radians). The coefficients generated that characterize the correction terms (truncated at second decimal) are -

$$
\begin{pmatrix}
A_1 & A_2 & A_3 & A_4 \\
B_1 & B_2 & B_3 & B_4 \\
C_1 & C_2 & C_3 & C_4 \\
D_1 & D_2 & D_3 & D_4
\end{pmatrix}
=
\begin{pmatrix}
-1.38 \times 10^{-8} & 1.26 \times 10^{-7} & -4.01 \times 10^{-7} & 4.59 \times 10^{-7} \\
3.18 \times 10^{-6} & -2.82 \times 10^{-5} & 8.60 \times 10^{-5} & -9.24 \times 10^{-5} \\
-1.93 \times 10^{-4} & 1.68 \times 10^{-3} & -4.98 \times 10^{-3} & 5.14 \times 10^{-3} \\
2.83 \times 10^{-3} & -2.44 \times 10^{-2} & 7.11 \times 10^{-2} & -7.02 \times 10^{-2}
\end{pmatrix}
$$

$$(2.25)$$

Notice the higher order correction terms are many orders of magnitude smaller than the linear and quadratic correction coefficients and, for parsimony, can be ignored. Lastly, before moving to polarization transport aspects of the calculation, we would like to mention that the most recent comprehensive review of various approximation methods to
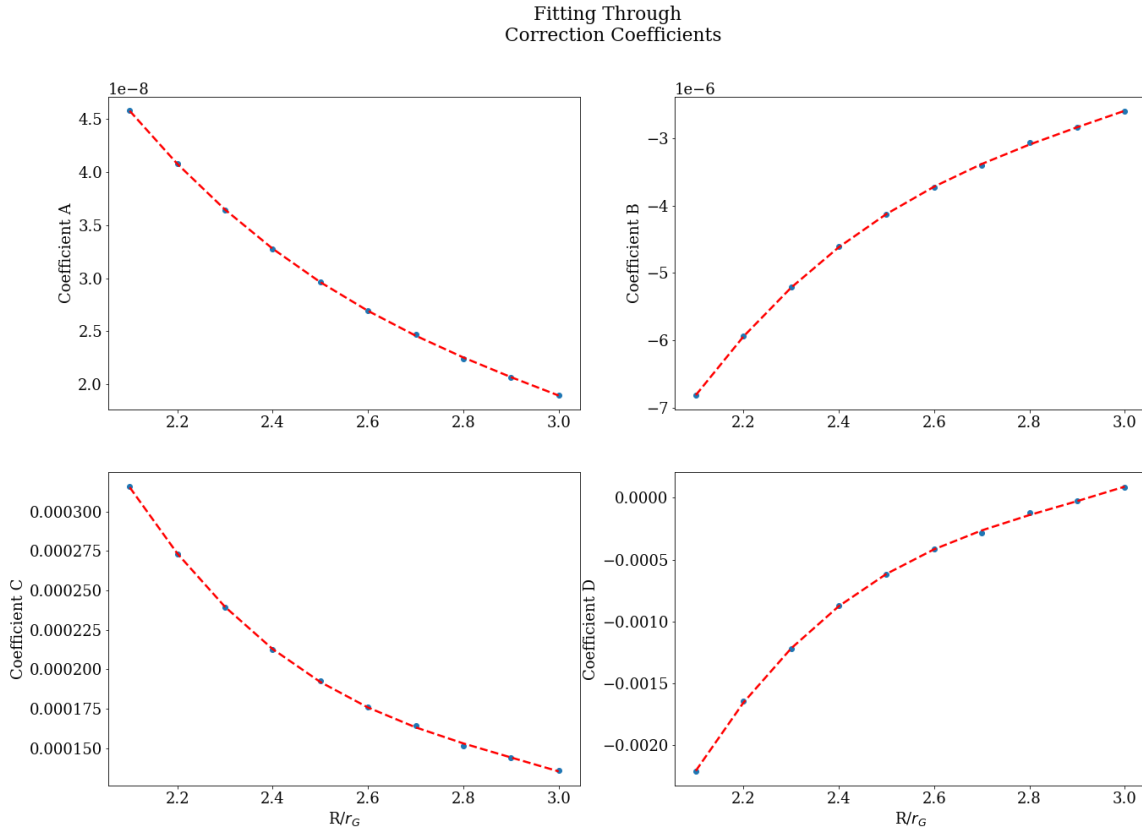
Figure 2.5: Coefficients characterizing the fit through Beloborodov approximation's residues follow a fourth-order polynomial sufficiently tightly. The coefficients of each individual fit are displayed in Eq. (2.25)

photon propagation can be found in [38].

## 2.4 Polarization Transport

We start with the assumption that the magnetic field of the neutron star can be approximated by a dipole $\hat{m}$ and that the star is asymmetric across $\hat{m}$. Though the degree of linear polarization is Lorentz invariant, polarization angle itself can depend on the choice of the basis in which one measures the Stokes parameters.

We define a coordinate system $(x, y, z)$ such that the z-axis points towards the line of sight (unlike Fig. 2.3 where x-axis was directed towards line of sight). Direction of $\hat{x}$ vector is fixed by the constraint that we want magnetic dipole $\hat{m}$ (sometimes referred to
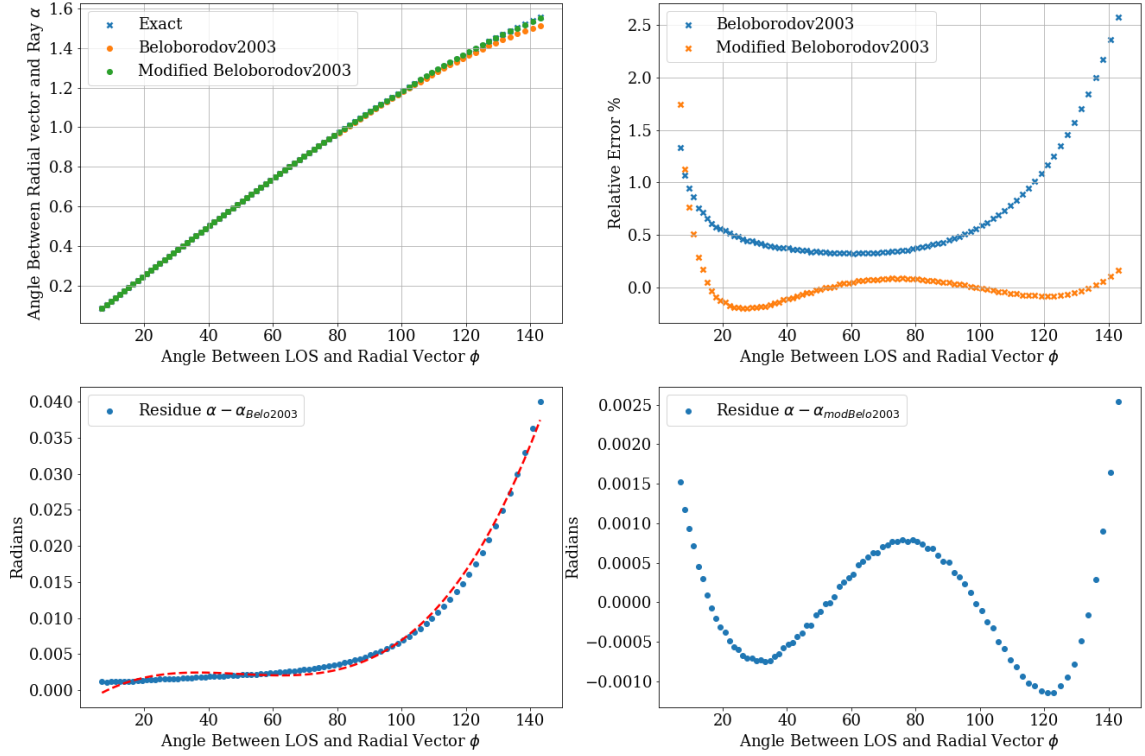
Figure 2.6: For $R = 2.1 r_G$, comparing exact results with approximations. The red line in bottom-left represents the fit through residues formed using the coefficients generated by the fits given in Fig. 2.5

as the axis of symmetry) to lie in the $x - z$ plane (see Fig. 2.8). This is the reference frame in which we will define the total flux $F_I$, flux in Q Stokes parameter $F_Q$ and U Stokes parameter $F_U$. The observed degree of linear polarization is defined (by convention) as

$$P_L = -\frac{F_Q}{F_I} \tag{2.26}$$

If the polarization is perpendicular to the projection of $\hat{m}$ in the sky-plane, we get $F_Q > 0$ and $P_L < 0$. Otherwise, for polarization parallel to the projection of $\hat{m}$ in the sky-plane, we have $F_Q < 0$ and $P_L > 0$. Since $\hat{z}$ is the direction of propagation of the radiation, there is no polarization along z-axis and $F_U$ component remains zero in this coordinate system. This is also follows from neglecting circular polarization. Further, $F_Q$ now be-
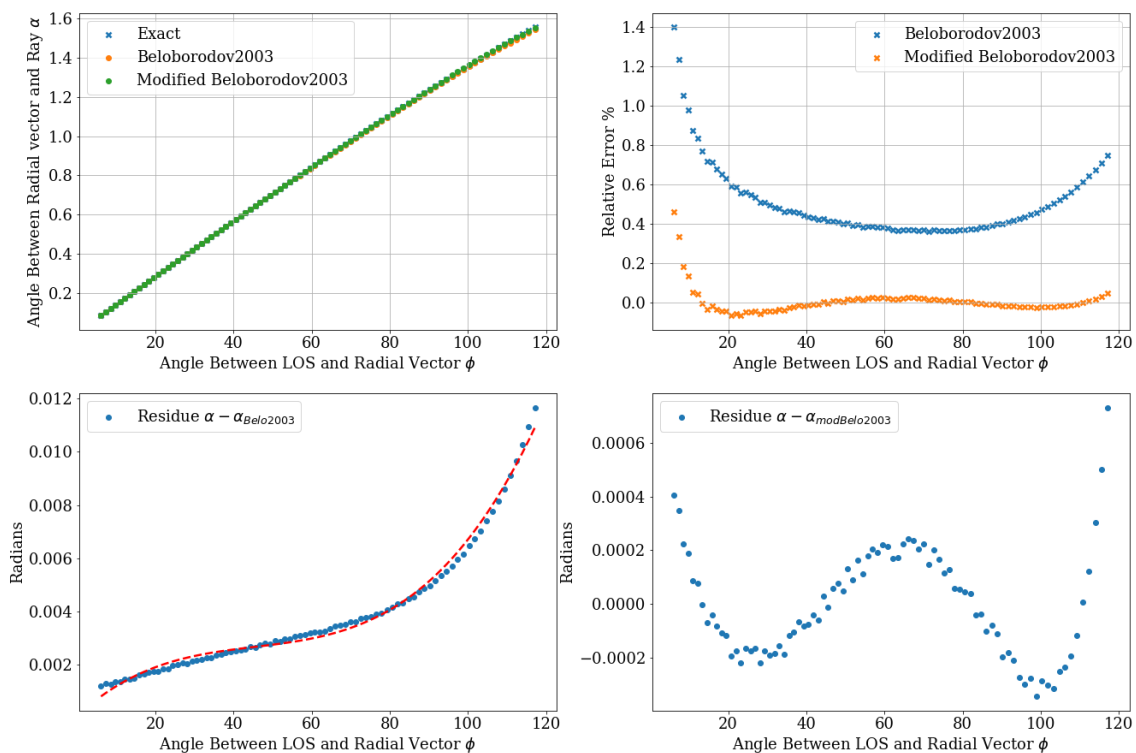
Figure 2.7: Same analysis as in Fig. 2.6 but now for $R = 3.0r_G$. Note for larger star radii, Beloborodov itself is a good approximation, though the correction term provide further improvements.

comes a function of the angle between line-of-sight and $\hat{m}$ because it characterizes the projection of $\hat{m}$ onto $\hat{x}$.

As we demonstrated in §2.3.2, the observed wave-vector (which is parallel to $\hat{z}$) is inclined at a bending angle $\beta$ with respect to the emitted wave-vector $\hat{k}'$. We found the bending angle $\beta = \phi - \alpha$ to be a function of the position of emission[3] $\phi$ and angle between $\hat{k}'$ and local normal $\hat{r}$ at emission point. We also found, in Schwarzschild geometry, $\phi$ always exceeds $\alpha$ leading to partial visibility of the 'back' hemisphere.

---

[3]In the coordinate system with $\hat{z}$ parallel to line of sight, $\phi$ becomes the co-latitude of the emission point (as opposed to being simply the latitude in earlier coordinate system).
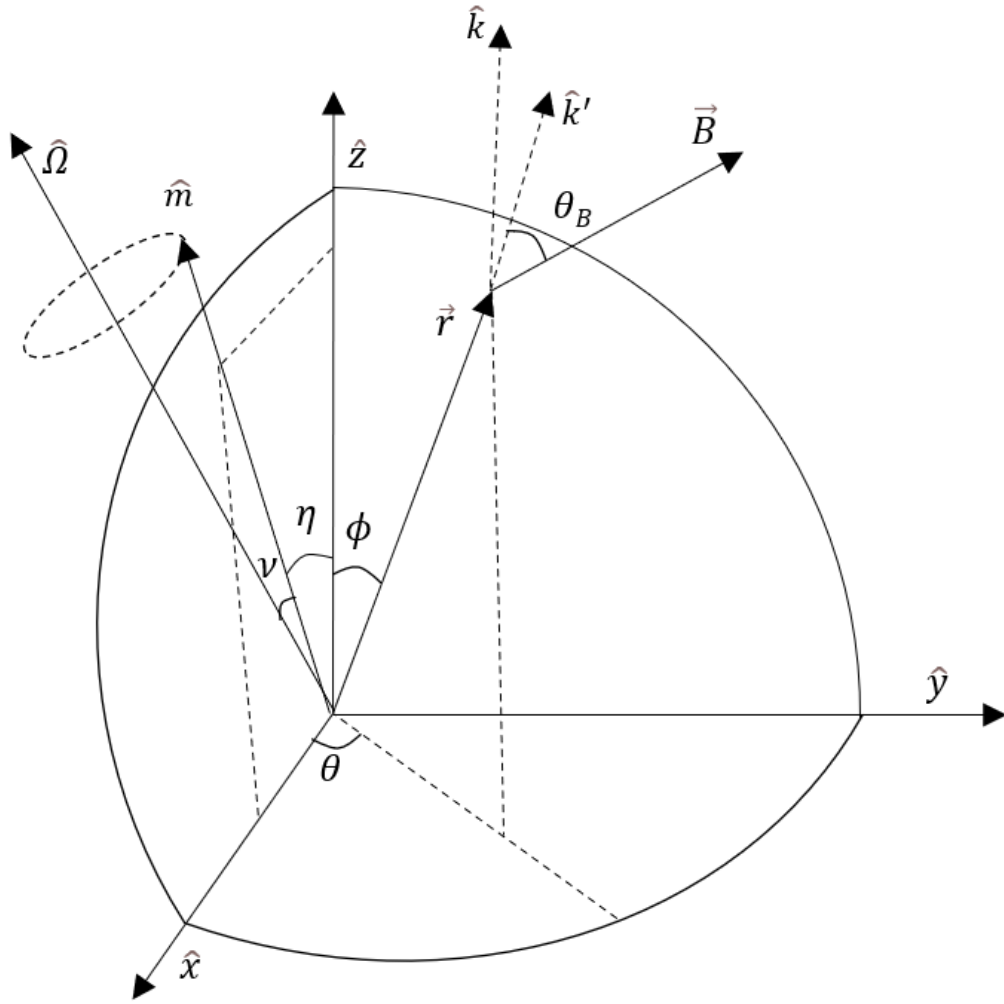
Figure 2.8: Un-primed global coordinate system $(x, y, z)$ with the magnetic dipole axis $\hat{m}$ on the $x - z$ plane and $\hat{z}$ pointing towards line of sight. $\hat{\Omega}$ is the rotation axis, $\eta$ is the angle between line of sight and magnetic dipole axis and $v$ is the angle between rotation axis and magnetic dipole axis.

### 2.4.1  Constraints on Polarization Parallel Transport

For discussions of polarization in GR contexts, it is helpful to remember that a polarization four-vector $\mathscr{E}^\mu$ (function only of 3-wavevector) can be defined using the solution for the electromagnetic four-potential $\mathscr{A}^\mu$ wave-equation.

$$\Box \mathscr{A}^\mu = 0 \implies \mathscr{A}^\mu = \mathscr{E}^\mu e^{-ik^\mu x_\mu} \tag{2.27}$$

33

But how is a spin-1 Boson described by the four-components of $\mathscr{E}^\mu$? This is possible because there are only two independent components of the photon polarization vector with others components being constrained by various gauge requirements. First, satisfying the Lorenz gauge condition leads to the following result which constraints the number of independent components to three.

$$\partial_\mu \mathscr{A}^\mu = 0 \implies k_\mu \mathscr{E}^\mu = 0 \tag{2.28}$$

This means the polarization four-vector remains orthogonal to the wave 4-vector. Then, exercising the additional gauge transformation

$$\mathscr{A}_\mu \to \mathscr{A}'_\mu = \mathscr{A}_\mu + \partial_\mu \Lambda \tag{2.29}$$

where $\Lambda$ is an arbitrary scalar that satisfies the wave-equation $\Box \Lambda = 0$ to ensure Lorenz gauge. We fix this scalar as

$$\Lambda = i a e^{i k^\mu x_\mu} \tag{2.30}$$

Considering that the following transformation (called the Coloumb gauge transformation) should also keep the physics unchanged

$$\mathscr{E}_\mu \to \mathscr{E}'_\mu = \mathscr{E}_\mu + a k_\mu \tag{2.31}$$

allows us to set $\mathscr{E}^0 = 0$ so that the Lorenz gauge condition can be written entirely in terms of the orthogonality of polarization and wave three-vectors.

$$\vec{k}.\vec{\mathscr{E}} = 0 \tag{2.32}$$

This polarization 4-vector $\mathcal{E}$ can now be parallel transported along a photon's null-geodesic to find how it transforms.

In 1975, Serge Pineault showed that the polarization vector, as measured by static observers, keeps a fixed orientation with respect to the angular momentum vector of the ray trajectory. This can be shown either through direct calculations (as done by Pineault in his PhD thesis) or by employing symmetry arguments [30]. Angular momentum vector here is defined as the normal to the plane of the ray-trajectory. Note that this assertion demands spherical symmetry because only then can we guarantee trajectories remain constrained on a plane. This result also implies that the polarization rotates in such a way that the angle with respect to the normal to trajectory plane remains conserved. This is an extremely helpful result because it means that nothing fundamentally changes in the plane where polarization bases are defined. It is the plane itself that rotates due to the bending of light. Without the bending of light, then, the angles $\chi_o$ and $\chi_e = \chi_o + \pi/2$ would also remain conserved. In fact, the observed angle of polarization in ordinary mode would precisely be the angle that the magnetic field $\vec{B}$ makes with the projection of $\hat{m}$ on the $x - y$ plane (i.e. the sky plane) since $\hat{z}$ is parallel to the rectilinear wave trajectory $\hat{k}$.

$$\chi_o^{obs} = \xi = \tan^{-1}(B_y/B_x) \tag{2.33}$$

### 2.4.2  Local Coordinate Frames

Now with the bending of light, we need to find how the orientation of the polarization plane changes. To begin, we define a new coordinate (local) system $(x', y', z')$ such that $\hat{z}'$ is parallel to the (bent) photon trajectory $\hat{k}'$ and the photon trajectory is constrained to the $x' - z'$ plane. Finally, $\hat{y}'$ is simply defined using the cross product of the two fixed unit vectors of this coordinate system (see Fig. 2.9). The connections between the local coordinate system (primed) with the global coordinate system (un-primed) can be made

using using just two angles.

1. $\cos\beta = \cos(\phi - \alpha) = \hat{k}.\hat{k}'$ defines the bending angle between a ray bent due to grav-
   itational effects and a ray propagating straight towards line of sight $\hat{z}$.

2. $\cos\theta = \hat{x}.\hat{x}' = \hat{y}.\hat{y}' = \hat{r}.\hat{x}$ is the azimuthal angle of the surface position vector $\vec{r}$
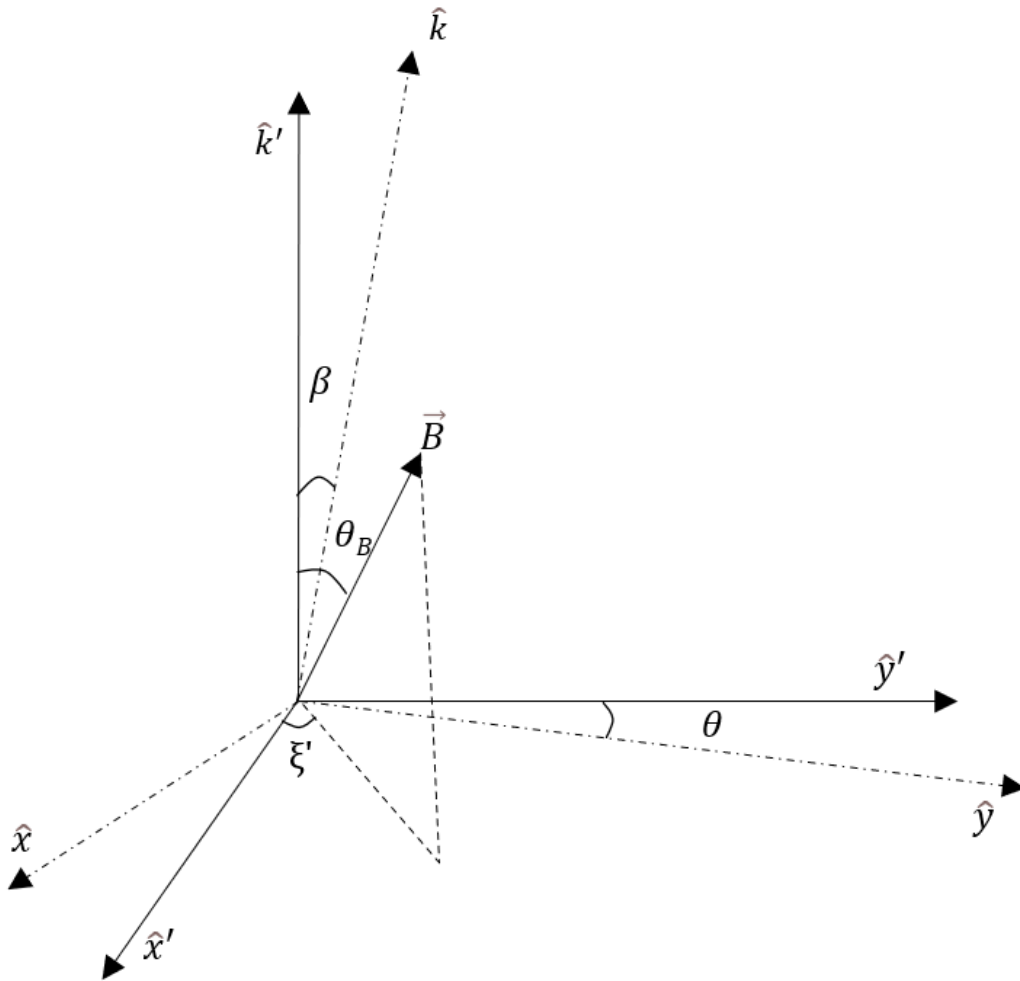   measured with respect to $x$-axis [27].



Figure 2.9: Primed local coordinate system $(x', y', z')$ defined on the neutron star surface
with $\hat{z}'$ pointing towards $\hat{k}'$. The photon trajectory is constrained on $x' - z'$ plane and $\theta$
is the azimuthal angle measured in the global coordinate frame.

This gives the transformation between the two coordinates as

$$\begin{pmatrix} \hat{x}' \\ \hat{y}' \\ \hat{z}' \end{pmatrix} = \begin{pmatrix} \cos\theta\cos\beta & \sin\theta\cos\beta & -\sin\beta \\ -\sin\theta & \cos\theta & 0 \\ \cos\theta\sin\beta & \sin\theta\sin\beta & \cos\beta \end{pmatrix} \begin{pmatrix} \hat{x} \\ \hat{y} \\ \hat{z} \end{pmatrix} \tag{2.34}$$

Now, using the knowledge that the angle between polarization vector and $\hat{y}'$ is conserved [30] and that polarization vector is perpendicular to $\hat{z}$ at the point of observation, we can relate the polarization of the emitted and the observed radiation via the simple expression [27]

$$\chi_o^{obs} = \xi' + \theta \tag{2.35}$$

where $\xi' = \tan^{-1}(B_{y'}/B_{x'})$ is the azimuthal angle that the projection of the magnetic field $\vec{B}$ onto the $x'-y'$ plane makes with the $\hat{x}'$. This angle $\xi$ depends on the bending angle $\beta$ and azimuthal location $\theta$. In large $R$ limit where GR effects are negligible, $\xi' \to \xi - \theta$ (and as expected from earlier results $\chi_o^{obs} \to \xi$).

### 2.4.3   Dipole Magnetic Field in Schwarzschild

To compute the angle $\xi'$, we need a model of how the magnetic field vector varies across the surface (for more details on magnetic fields on neutron stars [39]). As mentioned earlier, we start by approximating neutron star's magnetic field as a dipole. The Maxwell equations for a dipole source can then be solved in a Schwarzschild spacetime as prescribed in [27, 40, 41] to get

$$\vec{B} = \frac{B_P}{2}\left((2+f)(\hat{r}.\hat{m})\hat{r} - f\hat{m}\right) \tag{2.36}$$

where $B_P$ is the magnetic field strength at the poles of the dipole and $f$ is a parameter that arises due to GR effects and can be expressed in terms of the ratio $u = r_G/R$

$$f = 2\frac{u^2 - 2u - 2(1-u)\ln(1-u)}{(u^2 + 2u + 2\ln(1-u))\sqrt{1-u}} \tag{2.37}$$

In the non-relativistic case, $f$ becomes 1 and the field strength of the dipole at its equation becomes half of the field strength at its pole. Alternatively, we can define an angle $\cos\gamma = \hat{r}.\hat{m}$ and write the magnetic field in terms of its radial $B_r$ and tangential components $B_\theta$

$$B_r = B_p \cos\gamma \tag{2.38}$$

$$B_\theta = \frac{B_P}{2}f\sin\gamma \tag{2.39}$$

Since $f$ is positive definite, the action of GR correction on the magnetic field is simply to make the $\vec{B}$ field more tangential. For our calculations, it is more convenient to have a representation of $\vec{B}$ in terms of $(x, y, z)$ and $(x', y', z')$ instead of $\hat{r}$ and $\hat{m}$. These too can be found easily by noting

$$\hat{r} = \sin\phi\cos\theta\hat{x} + \sin\phi\sin\theta\hat{y} + \cos\phi\hat{z} \tag{2.40}$$

and for some given angle $\eta$ between line-of-sight and magnetic axis $\hat{m}$

$$\hat{m} = \sin\eta\hat{x} + \cos\eta\hat{z} \tag{2.41}$$

However, for a general rotating neutron star, the angle $\eta$ is a function of the spin phase and depends further on the offset of the magnetic axis $\hat{m}$ from the spin axis $\hat{\Omega}$. If we define the angle between line of sight $\hat{z}$ and neutron star spin axis $\hat{\Omega}$ as $\zeta$ and the angle between magnetic axis $\hat{m}$ and spin-axis $\hat{\Omega}$ as $\nu$, then the projection of the spin axis onto

line of sight changes as

$$\cos\eta = \cos\zeta\cos\nu + \sin\zeta\sin\nu\cos\Phi \tag{2.42}$$

where $\Phi$ is spin-phase of the neutron star. We can further write spin-phase as a function of time using the parameters angular velocity $\omega$ or pulsar period $T$ as

$$\Phi = \omega t = 2\pi(t/T) \tag{2.43}$$

## 2.5   Solving for Polarization Pulse Profiles

To finally model how polarization properties for neutron stars vary with spin-phase, we start by discretizing the neutron star surface into a mesh. Then, for each $(\phi, \theta)$ location, we find the corresponding $\alpha$ for that patch using the Beloborodov approximation Eq. 2.21 and the polynomial residue fit. Then, we calculate the unit radial vector $\hat{r}$ for that location patch. Using $\hat{r}$ (Eq. 2.40) and $\hat{m}$ (Eq. 2.41), we find $\vec{B}$ in primed coordinates (using Eq. 2.36) and, then, in un-primed coordinates (using Eq. 2.34). $\vec{B}$ in primed coordinates will help in calculating $\xi'$ which finally gives $\chi_o^{obs}$ (using Eq. 2.35).

Now, to compute the Stokes parameter, we need to calculate the normal mode's degree of linear polarization $p_L$ (using Eq. 2.5) which requires us to compute two more quantities - $\theta_B$ (angle between wave-vector $\hat{k}'$ and magnetic field $\vec{B}$) and $B$ (strength of the magnetic field). We do so using

$$\theta_B = \cos^{-1}(B_{z'}/B) \tag{2.44}$$

The strength of the magnetic field is computed (with GR corrections) using $\cos\gamma = \hat{r}.\hat{m}$

$$B = (B_P/2)\sqrt{(4 - f^2)\cos^2\gamma + f^2} \tag{2.45}$$

This is needed to find the cyclotron energy which goes into computing $q$ factor. Then, we integrate over the entire visible surface using the definition of Stokes parameter

$$F_Q = R^2 g_r \int_{-\pi/2}^{\pi/2} d\alpha \cos\alpha \int_0^{2\pi} d\theta (I_o - I_e) p_L \cos(2(\xi' + \theta)) \qquad (2.46)$$

where we have included additional gravitational redshift factor $g_r = \sqrt{1 - r_g/R}$ to account for the change in photon energy from emission $E'$ to observed $E$.

Finally, we repeat this process for the entire range of spin phase $\Phi$ to generate a pulse profile of flux observed in Q stokes parameter, which in turn provides us with the observed degree of linear polarization $P_L = -F_Q/F_I$. These calculations have been fed into the Polarization Transport Code (described in detail in the Appendix) and the results generated are discussed in the following chapter.

# Chapter 3

# Results of Polarization Transport

*In this chapter, we present the results generated by the Polarization Transport Code (which performs the calculations described in Chapter 2). The dependence of polarization pulse profiles for neutron star pulsars on characteristic angles (between dipole moment and spin axis ν and line of sight and spin axis ζ), compactness factor, magnetic field strength, photon energy and source function are discussed.*

## 3.1   Normal Mode Polarization

Before talking about how polarization gets transported and what pulse profiles an observer should expect, it is helpful to first discuss polarization of the emissions on the Neutron star's surface for the two normal modes $I_o$ and $I_e$. Following the discussion in §2.1, the degree of linear polarization for normal modes have been shown in Fig. 3.1. These results demonstrate that for photon energies lesser than the ion cyclotron energy ($E < 6.32(B/10^{15})$), the normal modes $I_o$ and $I_e$ remain linearly polarized for a wide range of angles. The dashed white lines represent the general order of magnitude of soft x-ray observations. While neutron stars with weaker magnetic fields would demonstrate highly polarized emissions in softer regimes of x-ray, neutron stars with strong magnetic

41

fields are great targets for polarimetery even in higher photon energies[1].
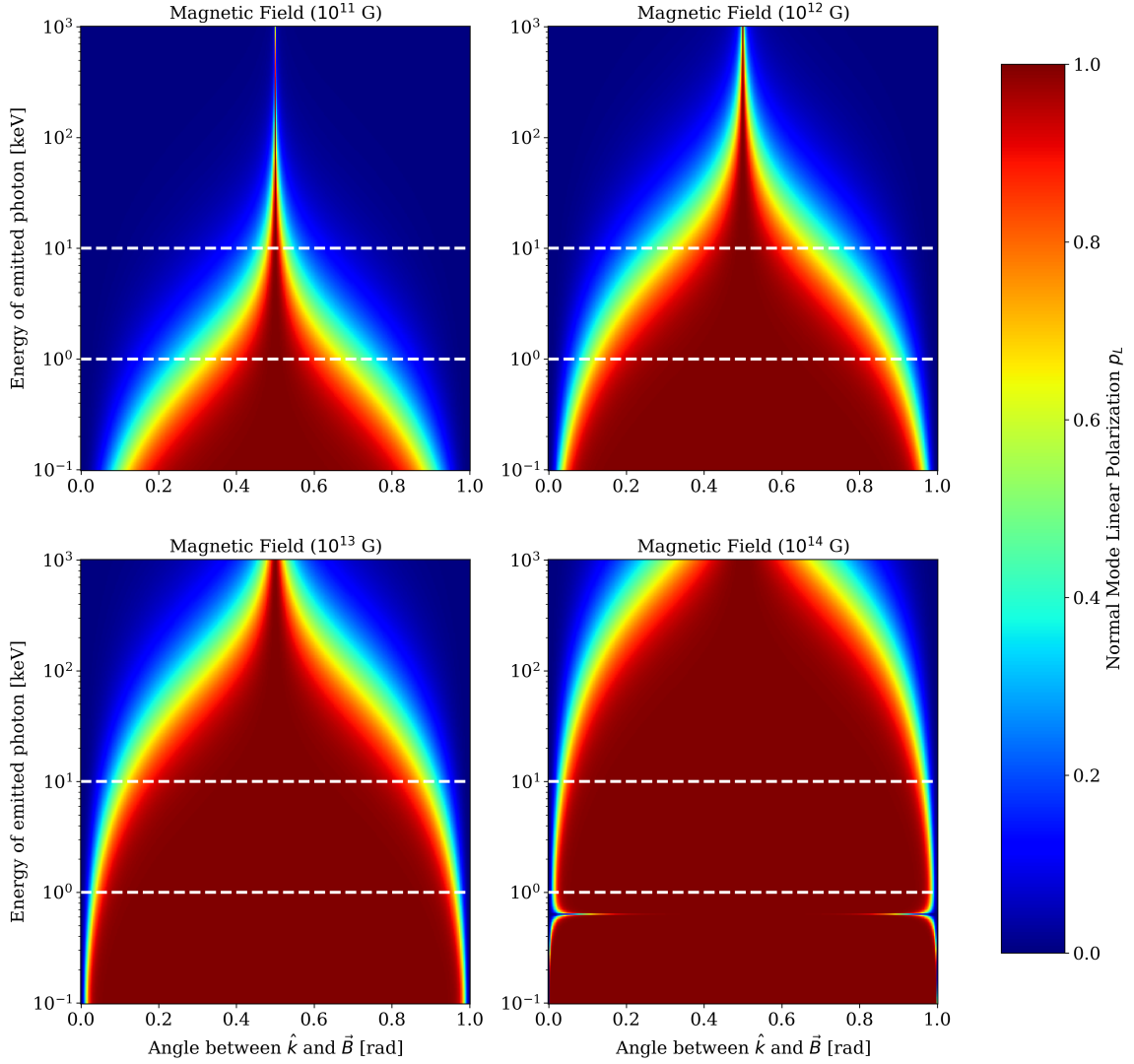


Figure 3.1: Degree of normal mode polarization shown for varying photon energies (as measured on neutron star surface before redshift) and angles $\theta_B$ between emitted photon and local magnetic field for four stars with different magnetic field strengths (as measured on the poles).

## 3.2 Geometry Dependence

Orientation of the magnetic dipole moment $\hat{m}$ and rotation axis $\hat{\Omega}$ with respect to the line of sight $\hat{z}$ can lead to drastically different pulse profiles, even if other physical pa-

---

[1]Note that this general trend gets disrupted for certain specific values of $B$, $E$ and $\theta_B$ (as show by the inward horizontal dips in last plot of Fig. 3.1). This is also discussed in [31].

rameters like field strength, compactness, etc. are held to be the same. In fact, on the basis of how many pulsar poles are visible to the observer, we can create four distinct categories of pulsars [37]. If we define an $\kappa$ and $\epsilon$ such that

$$\kappa \equiv \frac{r_G}{R - r_G} \qquad \epsilon = \cos^{-1} \kappa \qquad (3.1)$$

Then we get the following four possible pulsar categories depending on our line of sight's orientation with respect to spin axis and the angular offset between spin axis and magnetic dipole moment (see Fig. 3.2).

1. Type 1 ($\cos(\zeta - \nu) > \kappa$): One pole visible at all times. Antipodal pole never comes in view.

2. Type 2 ($-\kappa < \cos(\zeta + \nu) < \kappa < \cos(\zeta - \nu)$): One pole is visible at all times. Antipodal pole contributes to total flux for some fraction of the spin phase.

3. Type 3 ($\cos(\zeta + \nu) < -\kappa$): One pole moves out of view for some time followed by visibility of only the opposite pole.

4. Type 4 ($-\kappa < \cos(\zeta + \nu)$ or $\cos(\zeta - \nu) < \kappa$): Contributions from both poles are in view at all times.

Assuming isotropic emission from the neutron star surface purely in ordinary modes, polarization pulse profiles were generated. The effect on percentage modulus of degree of linear polarization due to varying characteristic angles in this simple emission model is displayed in Fig. 3.3.

Certain salient features of pulsar polarization observations become manifest naturally from these results. The maximum degree of linear polarization is achieved when the magnetic dipole moment is maximally offset by the spin axis at $90^o$. Further, if the dipole moment is parallel to the spin axis then the observer receives a constant degree of linear polarization throughout the spin phase evolution. The orange curve in top-right
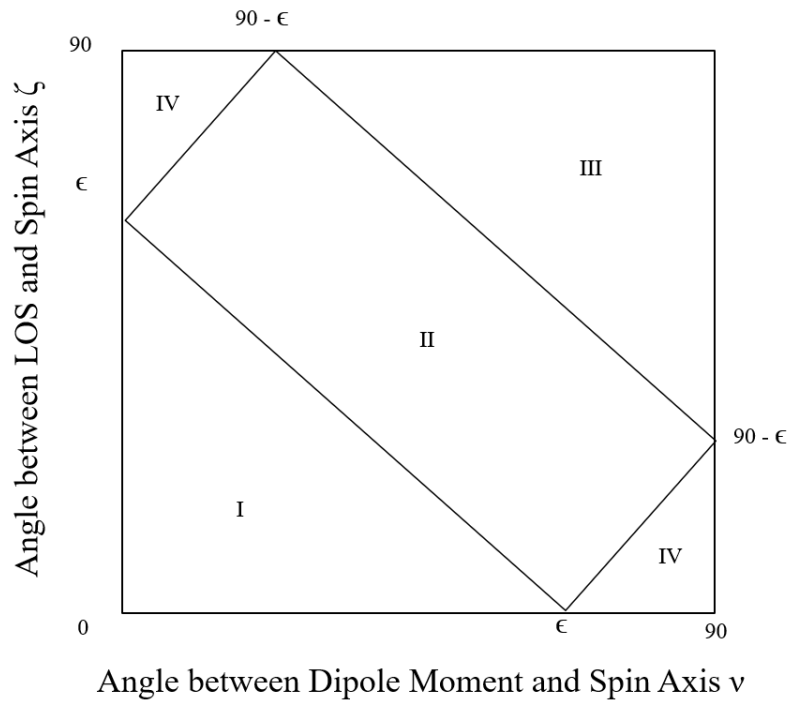
Figure 3.2: Depending on the characteristic angles and the compactness factor of the neutron star, observed pulsating flux may have contributions from only one pole at all times, both poles but with one pole contributing only for some part of the pulse, both poles but only one pole contributing at a time or both poles with each contributing at all times. This provides a natural classification of pulsars into Type 1, 2, 3 and 4 respectively.

plot in Fig. 3.3 is a pulsar of Type 1 (i.e. only one magnetic pole contributes towards the net polarization at all spin phases). In rest of the cases displayed in the figure, we see degree of linear polarization displays two maxima corresponding to the two magnetic poles. The maximum variation in degree of linear polarization is apparent when the dipole moment is maximally offset with respect to spin axis and line of sight is perpendicular to the spin axis. This means we see the polarization contributions from a magnetic poles during the maxima and during the minima both magnetic poles contribute minimally.

44

Figure 3.3: Polarization dependence on characteristic angles for a model neutron star emitting at constant intensity in purely ordinary mode. The compactness factor fixes the constants $\epsilon = 60^o$ and $\kappa = 0.5$.

## 3.3 Compactness Dependence

In a similar constant intensity in ordinary mode approximation, we will now vary the compactness and verify whether we can find signatures of the qualitative guess made in the previous chapter. For this examination, we fix the characteristic angles at $\nu = 45^o$ and $\zeta = 60^o$ and the maximum magnetic field strength at $10^{11}$ Gauss. The pulse profiles are generated for photon energy of 1KeV. From Fig. 3.4, we clearly see that changes in compactness create minimal changes in the visual appearance of the pulse profiles. However, on observing a zoomed in section of the pulse profile, it can be deduced that that bigger neutron stars (i.e. with lower compactness factor) reach higher degrees of linear polarization. This is compatible with the prediction made earlier that higher compactness would lead to more mixing of differently polarized emissions from the surface - leading to a decrease in the net linear polarization. Therefore, in principle, given a mechanism to estimate field strength and a radiative transfer model for NM polarization

in NS atmosphere and having performed pulse profile modelling to find characteristic angles, it is indeed possible to use polarimetric observations for putting a bound on the compactness factor of neutron stars.
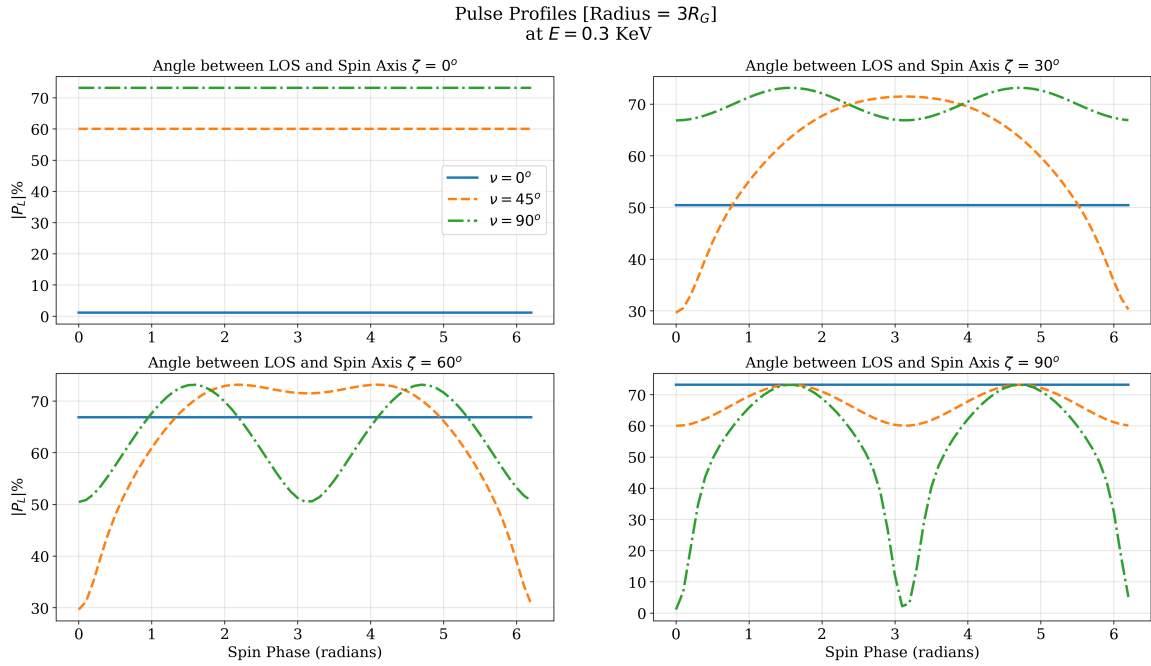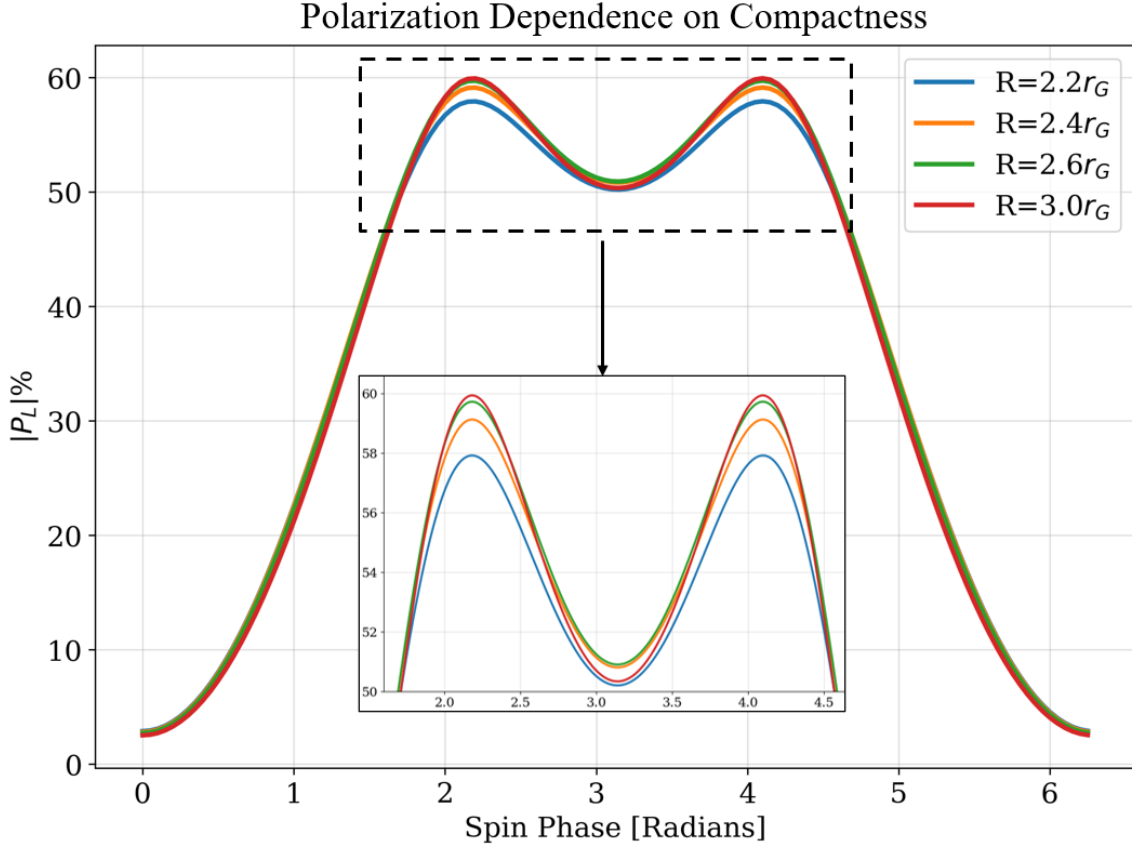


Figure 3.4: Polarization dependence on compactness for a model neutron star emitting at constant intensity in purely ordinary mode. The results are generated for $\kappa = 0.83, 0.71, 0.62, 0.5$. Since $\cos(\zeta + \nu) = -0.25$ and $\cos(\zeta - \nu) = 0.90$, all the profiles are for a Type III pulsar demonstrating two distinct maxima.

## 3.4 Magnetic Field Dependence

The effects of both magnetic field and photon energy can already be inferred from the results shown in Fig. 3.1. Stronger magnetic field strengths raise the ion cyclotron energy $E_{B_i}$. Therefore, if we restrict ourselves to observations in a particular photon energy, decreasing magnetic field would decrease the range of angles $\theta_B$ over which the normal modes become linearly polarized. We can verify these results through the polarization

profiles generated by varying magnetic fields for a star of radius $2.5r_G$ shown in Fig. 3.5 at photon energy of 1KeV. The pulses have been simulated for two complete rotations of the neutron star to show the periodicity of polarization variations more clearly in this case.
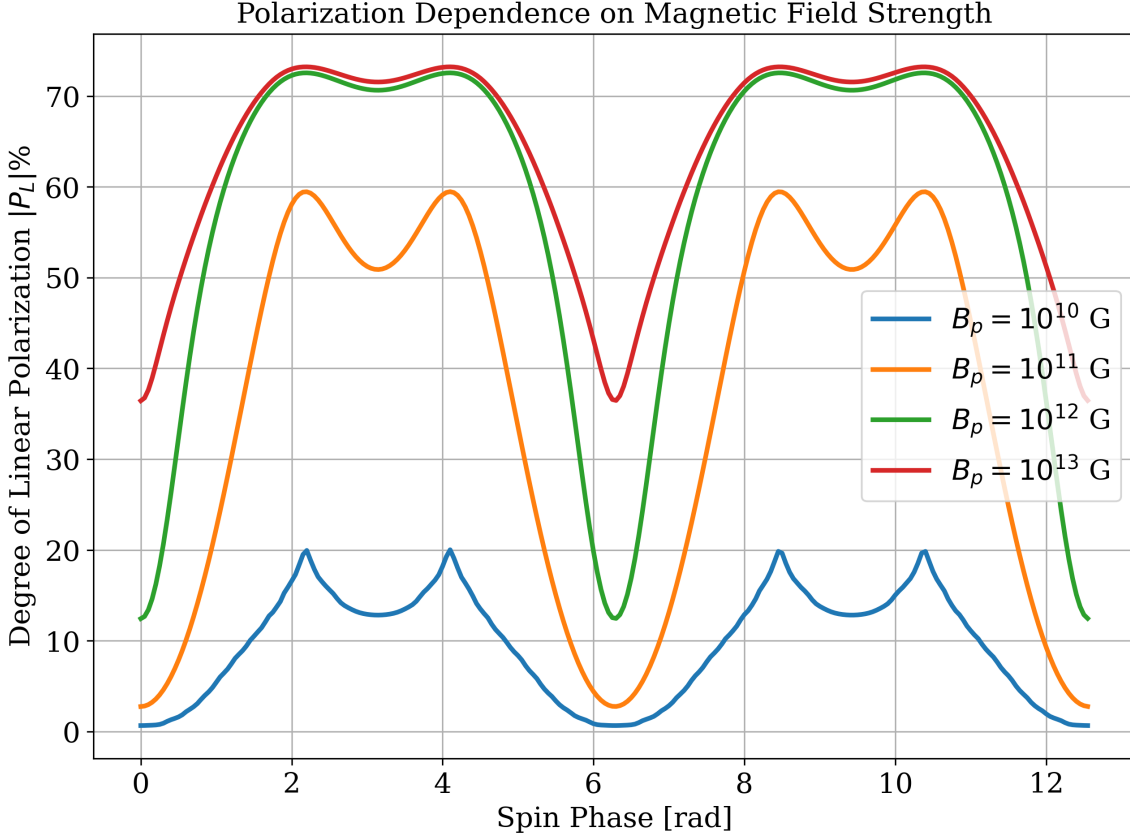


Figure 3.5: Variations in percentage degree of linear polarization calculated for two full rotations for constant emissions purely in ordinary modes (R = $2.5r_G$). Characteristic angles are fixed at $\nu = 45^o$ and $\zeta = 60^o$.

Immediately, from Fig. 3.5 we can infer that magnetic field strength raises both the maxima and minima of the degree of linear polarization a particular photon energy for some set characteristic angles. Another observation is that raising the magnetic field strength also 'smoothens' the variation in pulse profiles because a larger range of $\theta_B$ now leads to polarized normal mode emissions. Therefore, on summing up the polarization contributions from the surface patches, we find that each patch contributes its

polarization in a smoothly varying fashion as the field strength decays from the poles to the equator along with their $\cos \alpha$ projections. On the other hand, if we look at the lowest magnetic field strength that is calculated in the figure, we find signatures that resemble random fluctuations. Note that there is no stochasticity in our calculations. Yet, when ion-cyclotron energy becomes comparable to that of the relevant soft x-ray photons, normal modes are linearly polarized for some narrowly defined angles between emission and local magnetic field. This is also reflected globally in the (blue) pulse profile through its sharper maxima at specific rotation phases (as opposed to a smooth climb in stronger field simulations).

## 3.5   Photon Energy Dependence

Photon energy and magnetic fields are complimentary and enter into the polarization calculations in similar places. This is made clear if we look at the results generated for $R = 2.5 r_G$, $\nu = 45^o$ and $\zeta = 60^o$ in Fig. 3.6. We find that increasing the photon energy decreases the degree of linear polarization. We can interpret this results, further, by noting that we are looking at emissions due to scattering. It is the scattered bits of radiation that are linearly polarized and contribute towards the net linear polarization. However, as the photon energy increases, the scattering cross section decreases. Therefore, the linearly polarized contribution towards the net emission decreases with an increase in photon energy.

Additionally, it can be observed that the effects of increasing photon energy by an order of magnitude is precisely the same as decreasing the magnetic field strength by an order of magnitude (follows from the equation for normal mode polarization Eq. 2.5). Naturally, this behavior raises the concern about possible degeneracy in development of inference methods since two very different parameter choices yield precisely the same polarization profiles. A further narrowing down of the potential parameter space is made possible due to the fact that observations of the same object can be per-
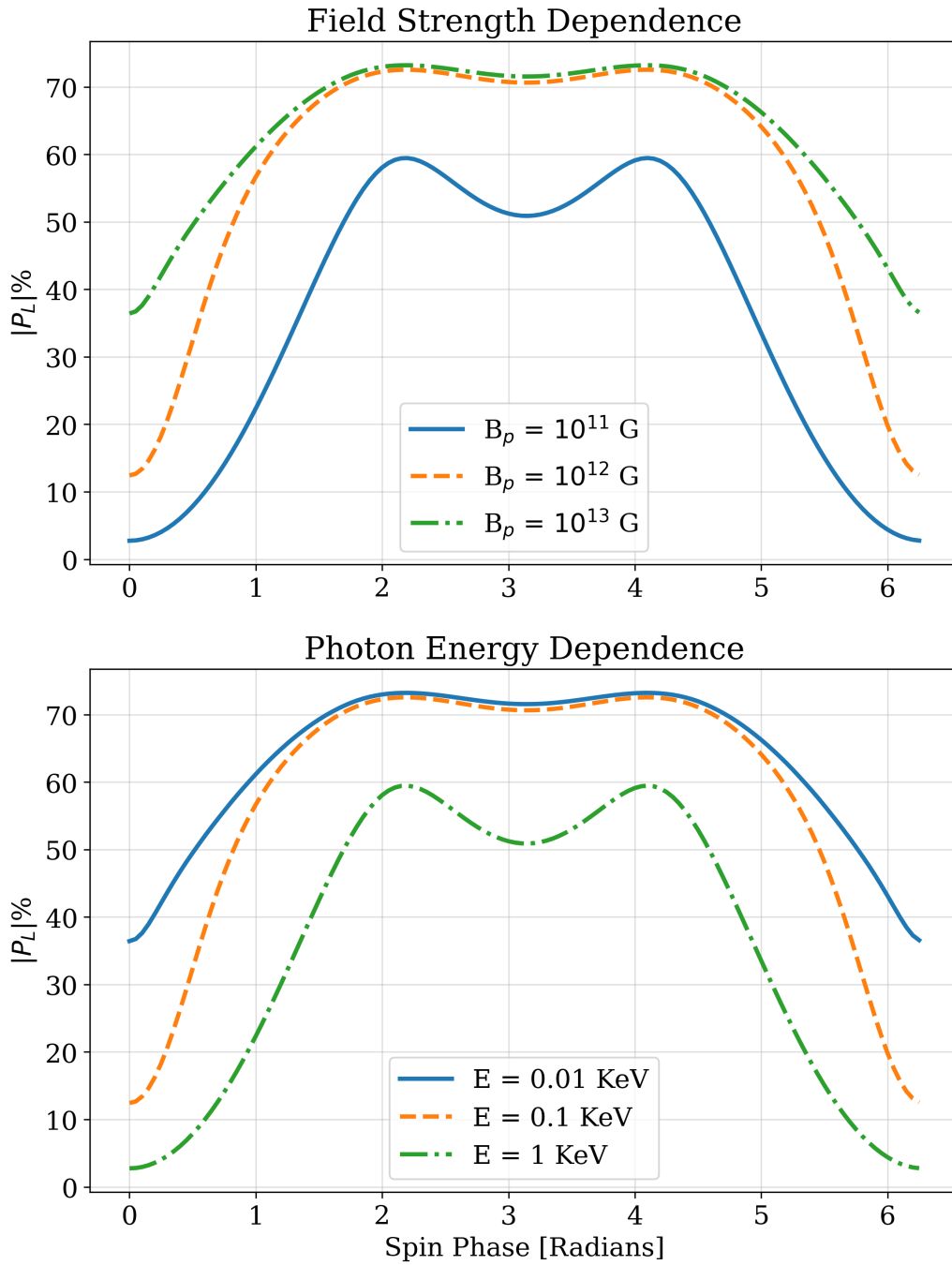
Figure 3.6: Results demonstrating the effects of varying magnetic field strength and photon energy on degree of linear polarization for fixed compactness and characteristic angles.
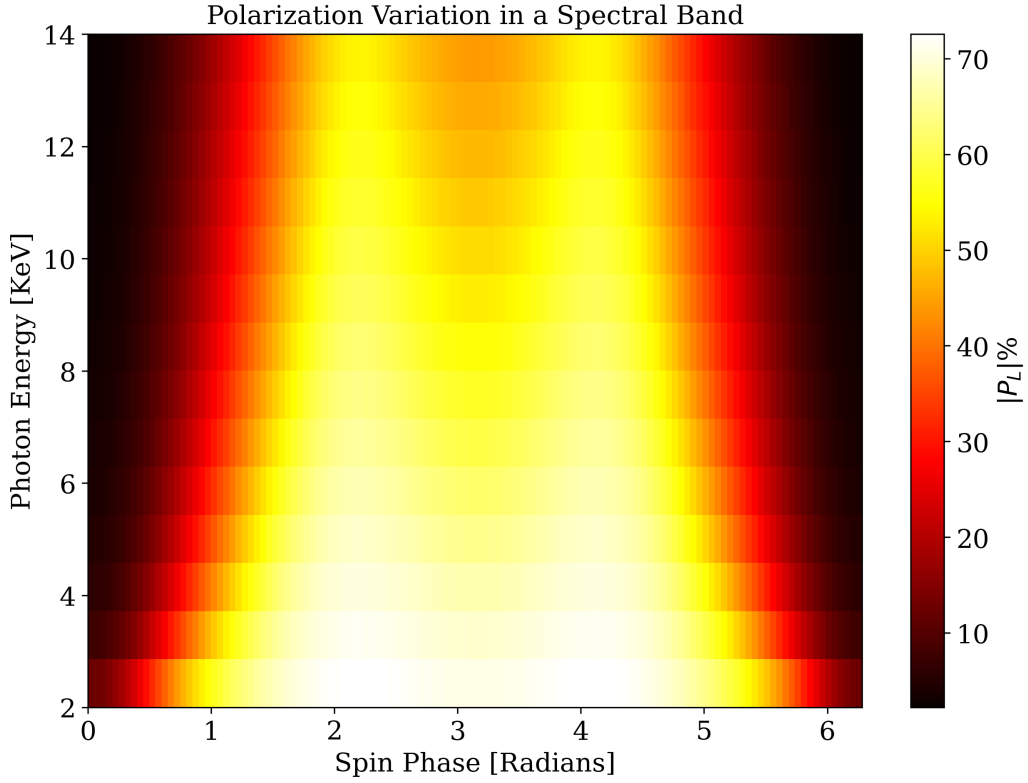
Figure 3.7: Simulated degree of linear polarization for a neutron star displayed as a heat-map across spin-phase and photon energy for an x-ray spectral band. Characteristic angles are fixed at $v = 45^o$ and $\zeta = 60^o$.

formed in a range of possible wavelengths. Thus, for any given object we have an entire family of pulse profiles. An example of such variations across a spectral band (assuming constant spectral intensity) is displayed in Fig. 3.7.

## 3.6 Source Function Dependence

Finally, the polarization pulse profiles must reflect features of intensity distribution across the normal modes and its spatial variation on the neutron star surface. In the results preceding this subsection, we had assumed constant emission intensity throughout the neutron star surface purely in ordinary modes. If we perform the same exercise but with purely extraordinary mode emissions, it follows from the definition of the Stokes parameters (Eq. (2.4)) that we would get the precisely the same kinds of variations in pulse

profiles but with a negative sign instead. As mentioned earlier, the sign of $P_L = -F_Q/F_I$ corresponds to the orientation of the observed polarization with respect to the plane of the sky. Since we have been plotting the modulus of the degree of linear polarization, all the graphs presented in this chapter would look precisely the same after swapping $I_o$ with $I_e$. However, in realistic settings, emissions are not purely in ordinary or extraordinary modes. Instead, there is a location dependence on these quantities which can be computed via radiative transfer calculations (see §4.1.1 for a quick overview).

Even without including radiative transfer, we can further study the dependence of polarization profiles by discarding out constant emission assumption. Two standard approaches are the Gaussian Hotspot model of surface emission and the Hollow Cone model of surface emission. In both these cases, $I_o$ and $I_e$ becomes functions of the cylindrical radius measured with respect to the magnetic dipole moment.

# Chapter 4

# Discussion and Conclusion

*In this chapter, we briefly discuss the possible directions in which the current project can be extended. This involves an elementary exposition of performing realistic radiative transfer calculations, solving for a neutron star metric, including effects of vacuum birefringence and adding Bayesian inference functionality. We end this chapter by mentioning two space-based missions (one active and one scheduled) which can provide observational insights relevant to the x-ray polarimetery of neutron star pulsars.*

## 4.1 Scope for Future Work

The current work on polarization transport near neutron stars can be extended in multiple directions, both in terms of doing more physics and adding further functionality. Some prospects for relevant extensions are discussed in the subsequent subsections.

### 4.1.1 Radiative Transfer

We have been working with simple source functions and emission models because we were primarily interested in the gravitational effects during the transport phase on the polarization vector. However, to more accurately model a realistic setting, we would like to employ our understanding of emission spectra in ordinary and extraordinary modes

and their variations with respect to surface location. These details can then be fed into the polarization transport code directly to generate the pulse profiles.

X-Ray emissions from neutron stars can be distinguished into non-thermal contributions (due to synchrotron and inverse Compton processes) and thermal contributions. Details on polarized radiation transfer in neutron star surface layers can be found in Barchas et al [42].

The general approach towards modelling NS atmospheres with and without inclusion of magnetic effects is broadly the same, except with magnetic fields present, we consider the polarization modes of radiation separately. This is important because radiative opacities depend on polarization. In such cases, the method of solving radiation transfer is described in §9.3.4 of [33]. Suppose the spectral intensity in two normal modes for frequency $\nu$ are $I_{\nu,1}$ and $I_{\nu,2}$. We write the following integro-differential equation

$$\mu \frac{d}{dz} I_{\nu,j}(\vec{n}) = k_{\nu,j}(\vec{n}) I_{\nu,j}(\vec{n}) - \left( \sum_{i=1}^{2} \oint d\vec{n}' I_{\nu,i}(\vec{n}') \sigma_{\nu,ij}(\vec{n}',\vec{n}) + \alpha_{\nu,j}(\vec{n}) \frac{B_\nu}{2} \right) \qquad (4.1)$$

where $\vec{n}$ is the unit wave-vector, $\sigma_{\nu,ij}$ is the scattering opacity from mode $i$ to $j$ (see [32] for more details), $k_{\nu,j} = \alpha_{\nu,j}(\vec{n}) + \sum_i \oint d\vec{n}' \sigma_{\nu,ij}(\vec{n}',\vec{n})$ is the total opacity, $\alpha_{\nu,j}$ is the absorption opacity for $j$ mode and $B_\nu$ is the Planck function. Next, we also assume that the atmosphere are radiative with the total energy flux being transferred solely through radiation and determined by effective surface temperature $T_{eff}$

$$\int_0^\infty d\nu \int_{-1}^{1} \mu I_\nu d\mu = \sigma_{SB} T_{eff}^4 \qquad (4.2)$$

where $\sigma_{SB}$ is the Boltzmann constant and $\mu$ is the projection factor of the local normal onto the wave-vector going outwards (see §**??**). Finally, we can also solve for the hydrostatic equilibrium of the atmosphere to get the variation of pressure with respect to

height $z$. In the plane-parallel approximation, this just becomes

$$p = gz \tag{4.3}$$

where $g$ is the acceleration due to gravity. To account for GR effects, this can be computed numerically. However, considering neutron star atmospheres are extremely thin, this is a good enough approximation. In practice, numerically solving radiative transfer equations happens in two-steps. First, one employs a diffusion approximation [33] and uses it to compute atmospheric structure. This solution is then fed into the exact equations and the process is repeated iteratively. Under right conditions, the algorithm relaxes to a solution of desired accuracy.

Computing spectral intensity of both thermal and non-thermal contributions in presence of very strong magnetic fields (which, for instance, would disturb the ionization equilibrium of NS atmospheric plasma) requires an involved effort. Codes have been developed which can perform such calculations efficiently (such as *MAGTHOMSCATT* [28]). Interfacing the polarization transport code with a radiative transfer module would then be a valuable extension to the current state of the project. Some additional information on models of magnetized neutron star atmosphere can be found in [43, 44] and radiative transfer calculations for neutron star mergers can be found in [45, 46].

### 4.1.2 Neutron Star Metric

As mentioned earlier, Schwarzschild metric only provides an approximation to the light-bending near neutron stars. A more complete approach towards the problem could start with, say, the Hartle-Thorne metric to first numerically solve for null-geodesics in it and then to compute the polarization parallel transport along those geodesics. The Hartle-Thorne metric [47] is the spacetime metric that describes the exterior geometry of a slow rotating rigid body. It is an approximation to the Kerr metric with the quadrupole

moment set to 0 (which is valid for black-holes but not in general). Following Hartle and Thorne, there were many more attempts to describe spacetime exterior to NS by analytic stationary and axissymetric metrics. Many of these attempts follow the algorithm to produce the metric using Ernst potential [48]. In 2016, Pappas proposed an accurate metric for exterior of neutron stars [49]. Another proposal for an all-purpose metric can be found in [50] (see [51] for further discussion on generating these metrics).

Choosing an appropriate metric is only the first step in solving the polarization transport problem. Once a metric is found, the next step is to find the equivalent photon-propagation equation. Without spherical symmetry, these photon orbits are not restricted to a plane anymore[1]. Then, for performing these computations in a reasonable amount of time on a personal computer, one must ideally search for an appropriate approximation (such as the one proposed by Beloborodov for Schwarszschild). It is only then that we would be ready solve the polarization transport problem in the more general metric.

### 4.1.3 Birefringence Through Distorted Fields

In our analysis, we have ignored the effects of vacuum birefringence. Vacuum birefringence is a prediction of Quantum Electrodynamics as per which, in the presence of magnetic fields stronger than a critical value $B_{QED} = 4.4 \times 10^{13} G$, vacuum itself acts a like birefringent medium and decouples the two polarization modes of the radiation passing through it. In other words, it means that the refractive index of one polarization mode differs (significantly) from the refractive index experienced by another polarization mode. For our analysis, this would imply a higher degree of linear polarization than expected for a given neutron star. Kubo and Nagata in 1983 showed that the polarization

---

[1]See this blog post by Leo C Stein for an interesting discussion on Kerr Photon Orbits

of wave travelling through a birefrigent and dichroic medium in geometric limit is

$$\frac{\partial \vec{s}}{\partial \lambda} = \hat{\Omega} \times \vec{s} + (\hat{T} \times \vec{s}) \times \vec{s} \tag{4.4}$$

where $\vec{s} = (Q/I, U/I, V/I)$ is the Stokes vector, $\lambda$ is the proper distance along the trajectory and $\hat{\Omega}$ and $\hat{T}$ are birefrigent and dichroic vectors respectively. Heyl et al. argue that on ignoring plasma and taking weak-field limit, dichroic vector vanishes [52]. The magnitude of the dichroic vector, then, becomes

$$|\hat{\Omega}| = \frac{2}{15} \frac{\eta}{4\pi} \frac{\omega}{c} \left(\frac{B_\perp}{B_{QED}}\right)^2 \tag{4.5}$$

where $B_\perp$ is the magnitude of that component of the magnetic field which is perpendicular to the direction of photon propagation and $\eta$ is the angle between line of sign and magnetic dipole vector $\hat{m}$. The birefringent vector $\hat{\omega}$ points towards the projection of magnetic field onto the Poincare sphere. These effects further morph the polarization information before it reaches an observer.

Magnetars are natural laboratories where one can test vacuum birefringence predictions. In fact, Migani et al in 2016 claimed to have presented present evidence of birebringence in optical polarimetery data of isolated neutron stars [53]. On the other hand, if this aspect of QED is to be trusted at face value, then inclusion of vacuum birefringence in our calculations can help in constraining the magnetic field strength of neutron stars. Therefore, an additional module that performs vacuum polarization calculations before generating the Stokes parameter pulse profiles would be a valuable addition. Further discussions on the topic of vacuum polarization in the context of neutron stars can be found in [29, 54].

### 4.1.4 Bayesian Inference

With the polarization transport code, we can predict what polarimetric data we would expect given a neutron star model. In practice, however, we are presented with the inverse problem i.e. to narrow down the space of possible models and see which parameters fit the observational data best. This is the domain of Bayesian inference and a sizeable fraction of computational astrophysicists working on pulsar data employ Bayesian techniques in their research[55, 56]. A helpful pedagogical introduction to Bayesian Inferences in the context of astrophysics can be found in [57]. The general idea is simply to employ the Bayes Theorem for conditional probabilities and compute Bayes factor for comparing between models. The Bayes Theorem states

$$P(\theta|Y) = \frac{P(Y|\theta)P(\theta)}{P(Y)} \tag{4.6}$$

where $P(Y|\theta)$ is the sampling distribution for some data $Y$ given the model $\theta$, $P(\theta)$ is the prior probability of the model itself and $P(Y)$ is the prior predictive probability (which is often ignored after the process of *marginalisation*). We use these to compute the *likelihood function $P(Y|\theta)$*.

The family of polarization profiles for a given object depends on many variables (like characteristic angles, surface polarization map, magnetic field variation, etc.) and, hence, sampling any sufficiently large parameter space to find the model best fitting the data becomes a very computationally challenging problem (see [58] for a brief review of various sampling techniques used to compute likelihood). Fortunately, generating polarization profiles is a problem that can be easily parallelized. On six-cores of a personal laptop, six polarization transport simulations can be run in parallel[2]. However, if one has access to appropriate computing resources (which further depends on how fine-grained the surface mesh is), instead of iterating through individual patches of the surface in a given spin phase, polarization contributions from all of the surface

---

[2]This is, in fact, how the polarization transport code is currently set-up to run

patches can be projected onto observer's location simultaneously. Further, if one has access to even better resources, all of the spin phases for a given star can be computed simultaneously too. These speed-ups would drastically improve the performance of an inference code and our ability to process through pulsar polarimetric data quickly. Such performance improvements and, later, interfacing with an inference engine could be yet another valuable extension of the program's current functionality.

## 4.2 Future Observations

The current analysis is only valid for isolated neutron stars. To date, we have found seven candidates for isolated X-Ray pulsars and they are informally called the 'Magnificent Seven' [59]. Performing polarimetery on X-Ray sources is, however, an experimental challenge (polarimetery requires a large number of photons) and we have only recently acquired the technological capacity to perform such studies. As of now, there are two relevant missions (one active and one planned) designed to acquire polarimetric data[3] which could be used in conjunction with Bayesian inference and the techniques described in this thesis. I discuss these briefly in the following subsections.

### 4.2.1 Imaging X-Ray Polarimetery Explorer (IXPE)

IXPE (Fig. 4.1) is a (relatively) small-scale NASA mission for studying polarization properties of astrophysical objects. Its primary observation targets are neutron stars, pulsar wind nebulae and black-holes, with a sensitivity in the 2-8 KeV range. It was launched on December 9, 2021 with a mission duration of 2 years and entered service on January 10, 2022. Initial results about birefringence from observations of 4U 012+61 have already been released [60]. Polarimetric resolution of IXPE is already a two order-of-magnitude

---

[3]In the meanwhile, before observational data from these missions becomes accessible to public, polarization transport code can generate mock data with varying amounts of stochasticity. This functionality was added to start developing a streamlined interface with some inference modules without having to wait for observational data.

improvement over its predecessor Orbiting Solar Observatory (OSO). IXPE employs a cloud-chamber imaging technique to measure polarization of incoming X-Ray photons, the details of which can be found in [61]. Another measurement of the core of Centaurus A suggested a low degree of linear polarization, which indicates radiation coming from scattering processes instead of accelerated charges in jets [62].
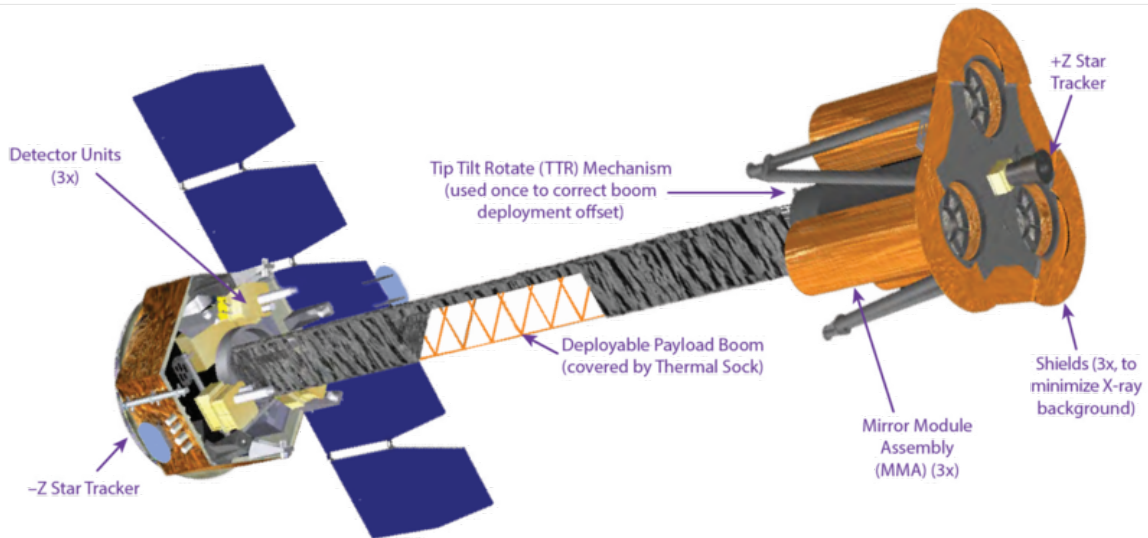


Figure 4.1: Schematic model of Imaging X-Ray Polarimetery Explorer showcasing its characteristic foldable boom arm. Image Credits: NASA

### 4.2.2 X-Ray Polarimeter Satellite (XPoSat)

Another observation mission relevant to our discussion is ISRO's XPoSat which is scheduled for launch in the second quarter of 2023 with a five year mission duration. It consists of two primary payloads - an X-Ray polarimeter (POLIX) and an X-Ray Spectroscopy and Timing instrument (XSPECT). POLIX would be measuring polarimetry parameters (both degree of polarization and angle) in medium x-ray range of 8-30 KeV photons. Unlike IXPE, polarimetery on board of XPoSat is performed via anisotropic Thompson scattering of incoming photons. As per the proposal, POLIX would provide first-ever views of more than 40 astrophysical objects in medium X-ray range.

## 4.3 Epilogue

Our understanding of high-energy phenomena in astrophysical contexts has largely developed through photometery, spectroscopy and gravitational interferometery. Both IXPE and XPoSat provide additional observational information on two novel parameters (degree of linear polarization and angle) to resolve certain degeneracies in the theoretical models of violent astrophysical phenomena. In the case of neutron star pulsars, however, we demonstrated mechanisms via which the observational data on polarization gets morphed. This understanding can aid in analysing the forthcoming data, reverse the gravitational morphing and predict what *actually* was emitted from the neutron star.

Neutron star polarimetery is a fertile field with an interesting theoretical past and an exciting observational future. We eagerly anticipate the insights this field will reveal about the fundamental nature of forces, interactions, and matter - about what is and is not permitted in our universe. We hope that observations of these exotic objects will fill us with awe and, yet, leave us pondering the mysteries that will confound astronomers, astrophysicists, and physicists alike. Above all, we await the answers that lie within the quanta of light, travelling across eons of space to reach us, illuminating secrets long hidden in the vast void.

# Bibliography

[1] S. L. Shapiro and S. A. Teukolsky, *Black holes, white dwarfs, and neutron stars: the physics of compact objects.* Wiley.

[2] V. L. Ginzburg, "PULSARS (theoretical concepts)," vol. 14, no. 2, pp. 83–103.

[3] "Neutron stars: Theory and observation."

[4] "Neutron stars and pulsars." OCLC: ocn305127637.

[5] D. G. Yakovlev, P. Haensel, G. Baym, and C. J. Pethick, "Lev landau and the conception of neutron stars," vol. 56, no. 3, pp. 289–295.

[6] R. C. Tolman, "Static solutions of einstein's field equations for spheres of fluid," vol. 55, no. 4, pp. 364–373.

[7] J. R. Oppenheimer and G. M. Volkoff, "On massive neutron cores," vol. 55, no. 4, pp. 374–381.

[8] S. Bowyer, E. T. Byram, T. A. Chubb, and H. Friedman, "Cosmic x-ray sources," vol. 147, no. 3656, pp. 394–398.

[9] A. M. W. Mitchell and J. Gelfand, "Pulsar wind nebulae," pp. 1–52.

[10] A. Hewish, S. J. Bell, J. D. H. Pilkington, P. F. Scott, and R. A. Collins, "Observation of a rapidly pulsating radio source," vol. 217, no. 5130, pp. 709–713.

[11] P. Haensel, A. Y. Potekhin, and D. G. Yakovlev, *Neutron stars. 1: Eqation of state and structure.* No. 326 in Astrophysics and space science library, Springer. OCLC: ocm75964765.

[12] D. Bhattacharya, "The formation of neutron stars in the galaxy," in *Neutron Stars: Theory and Observation* (J. Ventura and D. Pines, eds.), pp. 103–123, Springer Netherlands.

[13] J. P. Ostriker and J. E. Gunn, "On the nature of pulsars. i. theory," vol. 157, p. 1395.

[14] G. Baym, C. Pethick, and D. Pines, "Superfluidity in neutron stars," vol. 224, no. 5220, pp. 673–674.

[15] A. G. Lyne, B. Anderson, and M. J. Salter, "The proper motions of 26 PSR.," vol. 201, pp. 503–520. ADS Bibcode: 1982MNRAS.201..503L.

[16] D. Bhattacharya, "Evolution of neutron star magnetic fields," vol. 23, no. 1, pp. 67–72.

[17] G. Chanmugam and M. Maheswaran, "Spin-down of pulsars.," vol. 27, pp. 307–310. ADS Bibcode: 1975PASJ...27..307C.

[18] Z. Yue-zhu, F. Yan-yan, W. Yi-huan, Z. Cheng-min, Y. Shao-hua, P. Yuan-yue, G. Yuan-qi, and W. De-hua, "Spin-down of pulsars, and their electromagnetic and gravitational wave radiations," vol. 40, no. 2, pp. 210–219.

[19] I. Contopoulos and A. Spitkovsky, "Revised pulsar spin-down," vol. 643, no. 2, pp. 1139–1145.

[20] C. W. Misner, K. S. Thorne, and J. A. Wheeler, *Gravitation.* W. H. Freeman.

[21] H. Gao, S.-K. Ai, Z.-J. Cao, B. Zhang, Z.-Y. Zhu, A. Li, N.-B. Zhang, and A. Bauswein, "Relation between gravitational mass and baryonic mass for non-rotating and rapidly rotating neutron stars."

[22] G. F. Burgio, I. Vidana, H.-J. Schulze, and J.-B. Wei, "Neutron stars and the nuclear equation of state," vol. 120, p. 103879.

[23] L. M. Capparelli, A. Damiano, L. Maiani, and A. D. Polosa, "A note on polarized light from magnetars," vol. 77, no. 11, p. 754.

[24] J. D. Jackson, *Classical electrodynamics.* Wiley, 3rd ed ed.

[25] G. G. Stokes, "On the composition and resolution of streams of polarized light from different sources," vol. 9, p. 399. ADS Bibcode: 1851TCaPS...9..399S.

[26] W. H. McMaster, "Polarization and the stokes parameters," vol. 22, no. 6, pp. 351–362.

[27] G. G. Pavlov and V. E. Zavlin, "Polarization of thermal x-rays from isolated neutron stars," vol. 529, no. 2, pp. 1011–1018.

[28] K. Hu, M. G. Baring, J. A. Barchas, and G. Younes, "Intensity and polarization characteristics of extended neutron star surface regions," vol. 928, no. 1, p. 82.

[29] R. Taverna, R. Turolla, D. Gonzalez Caniulef, S. Zane, F. Muleri, and P. Soffitta, "Polarization of neutron star surface emission: a systematic analysis," vol. 454, no. 3, pp. 3254–3266.

[30] S. Pineault, "Polarized radiation from a point source orbiting a schwarzschild black hole," vol. 179, no. 4, pp. 691–697.

[31] T. Bulik and G. Pavlov, "Polarization modes in a strongly magnetized hydrogen gas," vol. 469, p. 373.

[32] Y. N. Gnedin and G. G. Pavlov, "The transfer equations for normal waves and radiation polarization in an anisotropic medium," vol. 38, pp. 903–908. ADS Bibcode: 1974JETP...38..903G.

[33] V. E. Zavlin and G. G. Pavlov, "Modeling neutron star atmospheres."

[34] G. G. Pavlov, Y. A. Shibanov, and D. G. Yakovlev, "Quantum effects in cyclotron plasma absorption," vol. 73, no. 1, pp. 33–62.

[35] J. B. Hartle, *Gravity: an introduction to Einstein's general relativity.* Addison-Wesley.

[36] G. Muñoz, "Orbits of massless particles in the schwarzschild metric: Exact solutions," vol. 82, no. 6, pp. 564–573.

[37] A. M. Beloborodov, "Gravitational bending of light near compact objects," vol. 566, no. 2, pp. L85–L88.

[38] O. Semerák, "APPROXIMATING LIGHT RAYS IN THE SCHWARZSCHILD FIELD," vol. 800, no. 1, p. 77.

[39] S. Konar, "Magnetic fields of neutron stars," vol. 38, no. 3, p. 47.

[40] B. Narzilloev, J. Rayimbaev, A. Abdujabbarov, B. Ahmedov, and C. Bambi, "Dynamics of charged particles and magnetic dipoles around magnetized quasi-schwarzschild black holes," vol. 81, no. 3, p. 269.

[41] L. M. Ozernoy and B. V. Somov, "The magnetic field of a rotating cloud and magneto-rotational explosions," vol. 11, pp. 264–283. ADS Bibcode: 1971Ap&SS..11..264O.

[42] J. A. Barchas, K. Hu, and M. G. Baring, "Polarized radiation transfer in neutron star surface layers," vol. 500, no. 4, pp. 5369–5392.

[43] V. Suleimanov, A. Y. Potekhin, and K. Werner, "Models of magnetized neutron star atmospheres: thin atmospheres and partially ionized hydrogen atmospheres with vacuum polarization," vol. 500, no. 2, pp. 891–899.

[44] P. Meszaros, R. Novick, A. Szentgyorgyi, G. A. Chanan, and M. C. Weisskopf, "Astro-physical implications and observational prospects of x-ray polarimetry," vol. 324, p. 1056.

[45] M. Tanaka and K. Hotokezaka, "RADIATIVE TRANSFER SIMULATIONS OF NEU-TRON STAR MERGER EJECTA," vol. 775, no. 2, p. 113.

[46] C. E. Collins, A. Bauswein, S. A. Sim, V. Vijayan, G. Martínez-Pinedo, O. Just, L. J. Shingles, and M. Kromer, "3d radiative transfer kilonova modelling for binary neu-tron star merger simulations," vol. 521, no. 2, pp. 1858–1870.

[47] J. B. Hartle and K. S. Thorne, "Slowly rotating relativistic stars. II. models for neutron stars and supermassive stars," vol. 153, p. 807. ADS Bibcode: 1968ApJ...153..807H.

[48] F. J. Ernst, "New formulation of the axially symmetric gravitational field problem," vol. 167, no. 5, pp. 1175–1178.

[49] G. Pappas, "An accurate metric for the spacetime around neutron stars," p. stx019.

[50] G. Pappas and T. A. Apostolatos, "An all-purpose metric for the exterior of any kind of rotating neutron star," vol. 429, no. 4, pp. 3007–3024.

[51] F. Frutos-Alfaro, "Approximate spacetime for neutron stars," vol. 51, no. 3, p. 46.

[52] J. S. Heyl, N. J. Shaviv, and D. Lloyd, "The high-energy polarization-limiting radius of neutron star magnetospheres – i. slowly rotating neutron stars," vol. 342, no. 1, pp. 134–144.

[53] R. P. Mignani, V. Testa, D. González Caniulef, R. Taverna, R. Turolla, S. Zane, and K. Wu, "Evidence for vacuum birefringence from the first optical-polarimetry mea-surement of the isolated neutron star RX j1856.53754," vol. 465, no. 1, pp. 492–500.

[54] A. Pérez Martínez, M. Pérez-Garcia, E. Rodríguez Querts, and A. Romero Jorge, "Vacuum properties and astrophysical implications," in *The Sixteenth Marcel Grossmann Meeting*, pp. 3756–3761, WORLD SCIENTIFIC.

[55] R. M. Marinho, H. O. De Oliveira, N. S. Magalhães, R. Valentim, J. G. Coelho, and M. E. S. Alves, "Bayesian inference applied to pulsar's models," vol. 45, p. 1760038.

[56] S. J. Vigeland and M. Vallisneri, "Bayesian inference for pulsar-timing models," vol. 440, no. 2, pp. 1446–1457.

[57] G. M. Eadie, J. S. Speagle, J. Cisewski-Kehe, D. Foreman-Mackey, D. Huppenkothen, D. E. Jones, A. Springford, and H. Tak, "Practical guidance for bayesian inference in astronomy."

[58] M. Y. Wang and T. Park, "A brief tour of bayesian sampling methods," in *Bayesian Inference on Complicated Data* (N. Tang, ed.), IntechOpen.

[59] A. Treves, S. B. Popov, M. Colpi, M. E. Prokhorov, and R. Turolla, "The magnificent seven: Close-by cooling neutron stars?."

[60] R. Taverna, R. Turolla, F. Muleri, J. Heyl, S. Zane, L. Baldini, D. G. Caniulef, M. Bachetti, J. Rankin, I. Caiazzo, N. Di Lalla, V. Doroshenko, M. Errando, E. Gau, D. Kırmızıbayrak, H. Krawczynski, M. Negro, M. Ng, N. Omodei, T. Tamagawa, K. Uchiyama, M. C. Weisskopf, I. Agudo, L. A. Antonelli, W. H. Baumgartner, R. Bellazzini, S. Bianchi, S. D. Bongiorno, R. Bonino, A. Brez, N. Bucciantini, F. Capitanio, S. Castellano, E. Cavazzuti, S. Ciprini, E. Costa, A. De Rosa, E. Del Monte, L. Di Gesu, A. Di Marco, I. Donnarumma, M. Dovčiak, S. R. Ehlert, T. Enoto, Y. Evangelista, S. Fabiani, R. Ferrazzoli, J. A. Garcia, S. Gunji, K. Hayashida, W. Iwakiri, S. G. Jorstad, V. Karas, T. Kitaguchi, J. J. Kolodziejczak, F. La Monaca, L. Latronico, I. Liodakis, S. Maldera, A. Manfreda, F. Marin, A. Marinucci, A. P. Marscher, H. L. Marshall, G. Matt, I. Mitsuishi, T. Mizuno, S. C.-Y. Ng, S. L. O'Dell, C. Oppedisano, A. Papitto,

G. G. Pavlov, A. L. Peirson, M. Perri, M. Pesce-Rollins, M. Pilia, A. Possenti, J. Pouta-nen, S. Puccetti, B. D. Ramsey, A. Ratheesh, R. W. Romani, C. Sgrò, P. Slane, P. Sof-fitta, G. Spandre, F. Tavecchio, Y. Tawara, A. F. Tennant, N. E. Thomas, F. Tombesi, A. Trois, S. Tsygankov, J. Vink, K. Wu, and F. Xie, "Polarized x-rays from a magnetar," vol. 378, no. 6620, pp. 646–650.

[61] A. Manfreda, "The gas pixel detectors for the imaging x-ray polarimetry explorer mission," vol. 1049, p. 168044.

[62] S. R. Ehlert, R. Ferrazzoli, A. Marinucci, H. L. Marshall, R. Middei, L. Pacciani, M. Perri, P.-O. Petrucci, S. Puccetti, T. Barnouin, S. Bianchi, I. Liodakis, G. Madejski, F. Marin, A. P. Marscher, G. Matt, J. Poutanen, K. Wu, I. Agudo, L. A. Antonelli, M. Ba-chetti, L. Baldini, W. H. Baumgartner, R. Bellazzini, S. D. Bongiorno, R. Bonino, A. Brez, N. Bucciantini, F. Capitanio, S. Castellano, E. Cavazzuti, S. Ciprini, E. Costa, A. De Rosa, E. Del Monte, L. Di Gesu, N. Di Lalla, A. Di Marco, I. Donnarumma, V. Doroshenko, M. Dovčiak, T. Enoto, Y. Evangelista, S. Fabiani, J. A. Garcia, S. Gunji, K. Hayashida, J. Heyl, W. Iwakiri, S. G. Jorstad, V. Karas, T. Kitaguchi, J. J. Kolodziejczak, H. Krawczynski, F. La Monaca, L. Latronico, S. Maldera, A. Man-freda, F. Massaro, I. Mitsuishi, T. Mizuno, F. Muleri, M. Negro, C.-Y. Ng, S. L. O'Dell, N. Omodei, C. Oppedisano, A. Papitto, G. G. Pavlov, A. L. Peirson, M. Pesce-Rollins, M. Pilia, A. Possenti, B. D. Ramsey, J. Rankin, A. Ratheesh, R. W. Romani, C. Sgrò, P. Slane, P. Soffitta, G. Spandre, T. Tamagawa, F. Tavecchio, R. Taverna, Y. Tawara, A. F. Tennant, N. E. Thomas, F. Tombesi, A. Trois, S. Tsygankov, R. Turolla, J. Vink, M. C. Weisskopf, F. Xie, S. Zane, J. Rodi, E. Jourdain, and J.-P. Roques, "Limits on x-ray polarization at the core of centaurus a as observed with the imaging x-ray polarimetry explorer," vol. 935, no. 2, p. 116.

# Appendix A

# Polarization Transport Code

All results generated in this thesis can be replicated using the Polarization Transport Code, which is available on this GitHub repository. The repository also contains simulated data which was generated as a part of this project. In this appendix, I provide a top-level user-guide for the polarization transport code.

The general workflow involving the polarization transport code is presented in Fig. A.1. We start by choosing a neutron star object from `starcatalog.py`. We feed this object to the functions defined in `polarizationtransport.py`. This is the part of the code which contains majority of the involved physics. We then perform a 'virtual observation' of this neutron star object by declaring how long do we want to simulate the pulse profile for, at what photon energy, etc. This would, then, produce the polarization profiles as seen in some given Stokes parameter.

The functions in `polarizationtransport.py` further call upon functions defined in `approximations.py` which primarily takes care of the lensing calculations using the modified Beloborodov approximation. It also calls `surfacemap.py` in case the user wishes to discharge the constant intensity assumption and work with the Gaussian Polarcap or Hollow Cone model of spatial intensity distribution.

The code utilizes python's `multiprocessing` functionality to parallelize the virtual observations. In most of the Jupyter notebooks on the repository, the code is configured
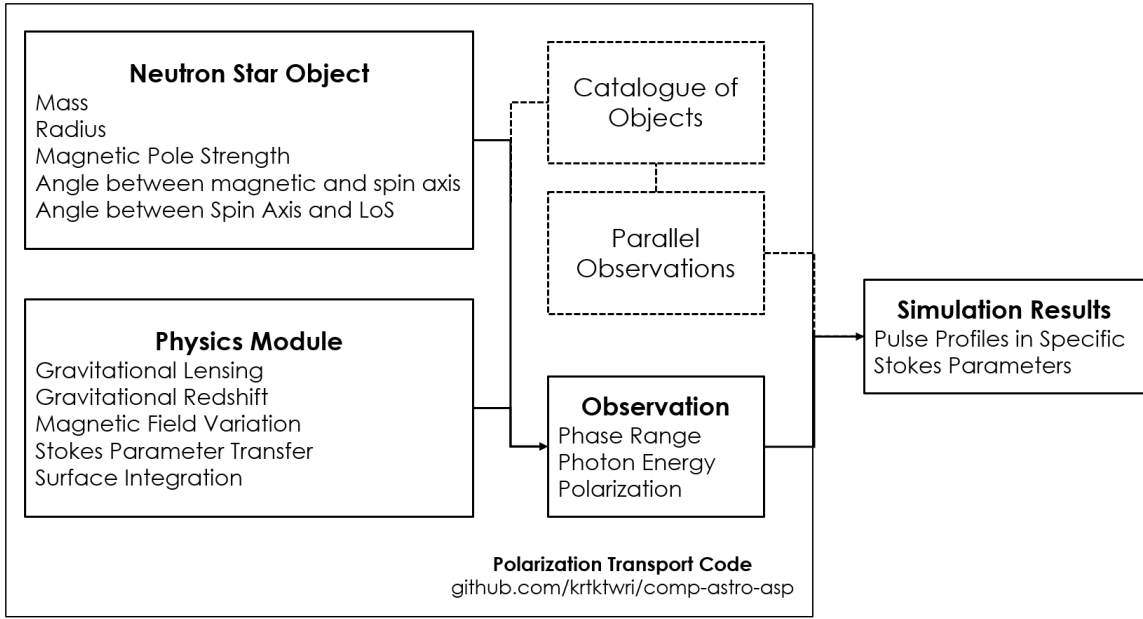
Figure A.1: Top-level schematic of the workflow with Polarization Transport Code

to utilize six cores of a personal laptop to perform six observations in parallel. However, depending on the available computing resources, one can modify this easily and perform as many parallel observations as desired.

Some important and frequently called objects in the code are summarized below -

1. `star(R, M, ν, ζ, `$B_p$`)`: Defines a neutron star object with a given radius (in units of $r_G$), mass (in units of $M_\odot$), angle between magnetic and spin axis, angle between line of sight and spin axis and magnetic field strength at the poles (in units of $10^{12}$ Gauss).

2. `stokes(phase, star, E, res='low')`: Calculates the Stokes parameter for a neutron star object at a given spin phase and photon energy. The resolution of the surface grid is, by default, set to 'low' at 0.5 gradations in $\phi$ and $\theta$. However, this can be changed to 'high' which uses a grid resolution of 0.01 instead. It outputs an array consisting of flux in Q, U and I Stokes parameters.

3. `observation(star, phaseRange, E, I_map=[])`: Performs surface integration over the entirety of a declared phase range. User can provide a surface intensity

69

map for inclusion in the calculations. Otherwise, it assumes isotropic emission.

For convenience, a summary of the equations that power the physics module of the Polarization Transport Code has been presented in Fig. A.2. Finally, for completeness,



**Stokes Parameter**

$$Q = (I_o - I_e) p_L \cos 2\chi_o$$

**Normal Modes Polarization**

$$p_L = \frac{|q| \sin^2 \theta_B}{\sqrt{4 \cos^2 \theta_B + q^2 \sin^4 \theta_B}}$$

**Dipole in Schwarzschild**

$$\vec{B} = \frac{B_P}{2} \left( (2 + f)(\hat{r}.\hat{m})\hat{r} - f\hat{m} \right)$$

$$f = 2 \frac{u^2 - 2u - 2(1 - u) \ln(1 - u)}{(u^2 + 2u + 2 \ln(1 - u)) \sqrt{1 - u}}$$

**Gravitational Lensing**

$$\left( \frac{dr}{d\phi} \right)^2 = \frac{r^4}{l^2} \left( 1 - \frac{l^2}{r^2} + r_G \frac{l^2}{r^3} \right)$$

**Polarization Rotation**

$$\chi_o^{obs} = \xi' + \theta$$

$$\xi' = \tan^{-1}(B_{y'} / B_{x'})$$

**Coordinate Transform**

Global          Local

**Surface Integration**

$$F_Q = R^2 g_r \int_{-\pi/2}^{\pi/2} d\alpha \cos\alpha \int_0^{2\pi} d\theta (I_o - I_e) p_L \cos(2(\xi' + \theta))$$

**Projection Rotation**

$$\cos\eta = \cos\zeta \cos\nu + \sin\zeta \sin\nu \cos\Phi$$

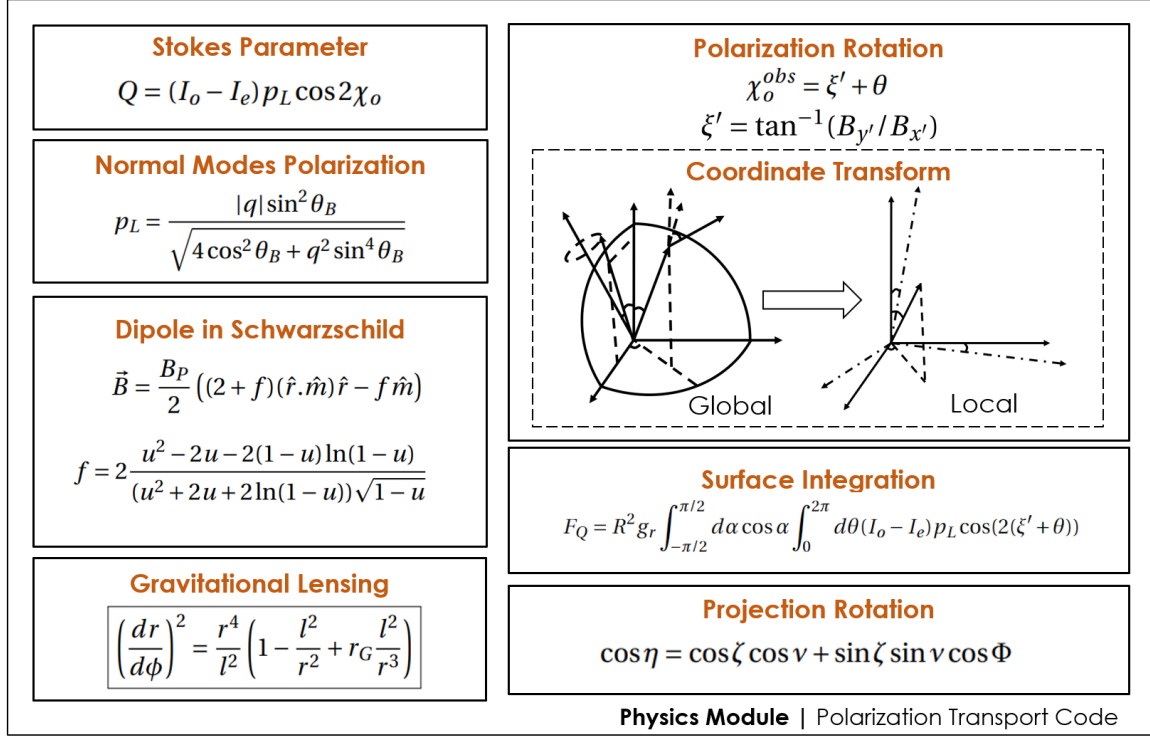**Physics Module** | Polarization Transport Code

Figure A.2: Important equations that are used by the physics module to perform polarization transport

following is the listing of the stokes() function which performs the calculations based on Fig. A.2 (for constant surface intensity).

```python
def stokes(phase, star, E, res='low'):

    if res == 'low':
        dtheta, dphi = 0.1, 0.1         # Low Resolution for testing
    else:
        dtheta, dphi = 0.05, 0.05       # Higher Resolution for final

    # unpacking star parameters
    R, star_nu, star_zeta, B_p = star.radius, star.nu, star.zeta, star.B_p
```

```
10
11     # extracting correction coefficients
12     corr_coeff = extract_coefficients(R)
13     phiLim = np.deg2rad(160)    # even in the most compact neutron
       stars (R = 2), lensing doesn't lead to seeing patches beyond 160
       deg
14
15     # Initializing Arrays
16     thetaRange = np.arange(0, np.pi, dtheta)
17     phiRange = np.arange(-phiLim, phiLim, dphi)
18
19     dA = R**2*dtheta*dphi        # unit area element
20     eta = np.arccos(np.round((np.cos(star_nu)*np.cos(star_zeta) + np
       .sin(star_nu)*np.sin(star_zeta)*np.cos(phase)), 12))
21
22     ## Defining m_hat vector components in x, y, z coordinates
23     m_hat = np.array([np.sin(eta), 0, np.cos(eta)])
24
25     # ratio R_g/R (R already in terms of schwarzschild radius)
26     u = 1/R
27     g_R = np.sqrt(1 - (u))    # gravitational redshift parameter
28
29     # GR correction to magnetic dipole moment
30     f = 2*(u**2 - 2*u - 2*(1-u)*np.log(1-u))/(np.sqrt(1-u)*(u**2 +
       2*u + 2*np.log(1-u)))
31
32     # empty list to store flux for each patch
33     FQ, FU, F = [], [], []
34
35     # from each alpha and theta
36     for i in range(0, len(thetaRange)):
37         for j in range(0, len(phiRange)):
38
```

71

```python
39          ## calculate psi (using belo function)
40          a = fastApprox((phiRange[j]), R, corr_coeff)[0]
41          beta = phiRange[j] - a
42          cosa = np.cos(a)
43
44          if cosa>0:
45              # computing trig functions once for each patch
46              costheta = np.cos(thetaRange[i])
47              sintheta = np.sin(thetaRange[i])
48              cosbeta = np.cos(beta)
49              sinbeta = np.sin(beta)
50              sinphi = np.sin(phiRange[j])
51              cosphi = np.cos(phiRange[j])
52
53              ### r_hat vector components in x, y, z coordinates
54              r_hat = np.array([sinphi*costheta,
55                                sinphi*sintheta,
56                                cosphi])
57
58              ### Defining component transformation matrix
59              T = np.array([[costheta*cosbeta, sintheta*cosbeta, -
    sinbeta],
60                            [-sintheta, costheta, 0],
61                            [costheta*sinbeta, sintheta*sinbeta,
    cosbeta]])
62
63              ## get magnetic field at all points
64              # in the basis vectors of (x,y,z)
65              B_vec = (B_p/2)*((2+f)*np.dot(r_hat, m_hat)*r_hat -
    f*m_hat)
66              # in the prime coordinates (x', y', z')
67              B_vec_prime = np.dot(T, B_vec)
68
```

```python
                ## find phi' using By' and Bx'.
                # phi' is the angle between the x' axis and the
    projection of B_vec_prime onto the x'y' plane
                xi_prime = np.arctan2(B_vec_prime[1], B_vec_prime
    [0])

                B = np.linalg.norm(B_vec)

                ## angle between magnetic field and the unit wave
    vector at the surface
                Theta_B = np.arccos(B_vec_prime[2]/B)

                # degree of linear polarization
                p_L = linear_polarization(Theta_B, B, g_R*E)

                ## compute flux in Q stokes parameter from this area
     element
                FQ.append(g_R*dA*cosa*(I_o-I_e)*p_L*np.cos(2*(
    thetaRange[i] + xi_prime)))
                FU.append(g_R*dA*cosa*(I_o-I_e)*p_L*np.sin(2*(
    thetaRange[i] + xi_prime)))
                F.append(g_R*dA*cosa*(I_o+I_e))


    return np.nansum(FQ), np.nansum(FU), np.nansum(F)
```